Tracking the evolution of the summit lava dome of Merapi volcano between 2018 and 2019 using DEMs derived from TanDEM-X and Pléiades data

Shan Grémion, Virginie Pinel, Tara Shreve, François Beauducel, Raditya Putra, Akhmad Solikhin, Agus Budi Santoso, Hanik Humaida

Tracking the evolution of the summit lava dome of Merapi volcano between 2018-2019 using DEMs derived from TanDEM-X and Pléiades data

Shan Grémion[1*], Virginie Pinel[1], Tara Shreve[2], François Beauducel[3], Raditya Putra[4], Akhmad Solikhin[4], Agus Budi Santoso[4], and Hanik Humaida[4]

(1) Université Grenoble Alpes, Université Savoie Mont Blanc, CNRS, IRD, Université Gustave Eiffel, ISTerre, Grenoble, France
*shan.gremion@univ-smb.fr
Université Savoie Mont Blanc, Campus Scientifique
73376 Le Bourget-du-Lac Cedex, France
(2) Earth and Planets Laboratory, Carnegie Institution for Science, Washington, DC, USA
(3) Université Paris Cité, Institut de Physique du Globe de Paris, CNRS, 75005 Paris, France
(4) Center for Volcanology and Geological Hazards Mitigation, Indonesia

At andesitic volcanoes, effusive lava flows and dome emplacement alternate with explosive, sometimes very destructive events. It is thus crucial to obtain quantitative information on the dome volume emplaced as well as on the extrusion rate. However, steep slopes and continuous activity make it difficult to install field instruments near many volcano summits. In this study, we take advantage of two high resolution remote-sensing datasets, Pléiades (optical acquisitions in tri-stereo mode) and TanDEM-X (radar acquisitions in bistatic mode), to produce twenty Digital Elevation Models (DEMs) over the summit area of Merapi volcano, Indonesia, between July 2018 and December 2019. We calculate the difference in elevation between each DEM and a reference DEM derived from Pléiades images acquired in 2013, in order to track the evolution of the dome in the crater. Uncertainties are quantified for each dataset by a statistical analysis of areas with no change in elevation. We show that the DEMs derived from Pléiades and TanDEM-X data are consistent with each other and provide good spatio-temporal constraints on the evolution of the dome. Furthermore, the remote-sensing estimate of the lava volume is consistent with local drone measurements carried out by BPPTKG at the time of dome growth. From our DEMs, we show that the dome growth was sustained by a relatively small effusion rate of about 0.0336 ± 0.0067 $m^3.s^{-1}$(2900 ± 580 m^3/day) from August 2018 to February 2019, when it reached a height of 40 meters (± 5 m) and a volume of 0.64 Mm^3 (± 0.03 Mm^3). The lava dome initially grew radially, and then extended asymmetrically to the northwest and southeast starting in October 2018. From February 2019 onwards, the dome elevation remained constant, but lava was continuously emitted. Lava supply was balanced by destabilization southwards downhill producing an accumulation zone of 400 meters long and maximum 15 meters (± 5m) high with a volume of 0.37 Mm^3 (± 0.29 Mm^3). The measured accumulation rate between February and September 2019 is 0.0094 ± 0.001 $m^3.s^{-1}$(810 ± 90 m^3/day). In late 2019, several minor explosions partially destroyed the center of the dome. This study highlights the strong potential of the joint use of TanDEM-X and Pléiades DEMs to quantitatively monitor domes at andesitic stratovolcanoes.

Keywords: TanDEM-X, bistatic interferometry, Pléiades, Digital Elevation Models (DEMs), lava dome volume, effusion rate

1. Introduction

On active stratovolcanoes, it is crucial to assess the hazard associated with the appearance of a new lava dome. Viscous lava domes build up by lava accumulation and eventually collapse when unstable (Harnett et al., 2018). During their collapse, they are either partially or totally destroyed, and sudden magma decompression might trigger explosions, volcanic blasts, ash plumes, pyroclastic density currents (PDCs) and lahars that might reach densely populated areas (e.g on Merapi, Voight et al., 2000 ; on Volcan de Colima, Capra et al., 2016; 2018). Frequently, a new dome appears after the destruction of the previous dome (e.g Zorn et al., 2019, Colima volcano between 2013-2015; Pallister et al., 2013, Merapi in 2010). The dome is often located in a crater surrounded by steep slopes : the growth of the dome can last weeks to years before being destroyed. Several potential causes have been suggested to explain the destruction of lava domes : a gravitational contribution due to oversteepened slopes of the dome, an over-pressure within or below the dome, or even external factors such as heavy rainfall (Kelfoun et al., 2021). However, the link between dome growth and collapse still remains to be solved. As a consequence, in the absence of obvious precursors to dome explosions, it is necessary to constantly evaluate the size and eruptive dynamics of the lava dome in order to evaluate the amount of magma that could be mobilized and to estimate the expected runout distance of potential dome-collapse PDCs.

Detection of variations of topography thanks to Digital Elevation Models (DEMs), volume estimates and changes in the effusion rate of the dome provide key information to evaluate the hazard and eventually raise alert levels (Fink and Griffith, 1998 ; Calder et al., 2002 ; Dietterich et al., 2021). Comparison of the effusion rate with historical records provides insights on changes to the dome and may also raise attention (Ogburn et al., 2015). Since 1000 AD, lava dome growth has occurred at one hundred and twenty volcanoes. Morphology, volume and effusion rates are then used to understand the behavior of such domes. Observational data are implemented in analogue (Donnadieu et al., 2003 ; Walter et al., 2022) or numerical modeling to understand dome destabilization (Harnett et al., 2018, 2021) , building (Walter et al., 2019) and strain evolution within the dome (Zorn et al., 2019 & 2020).

Topographic changes are mainly tracked using optical, radar and thermal infrared imagery when available : however, tracking changes is often challenging due to the small size of domes (between 100-200 m wide on average) often hosted within a summit crater of similar size. Both thermal and radar methods have the advantage of being able to provide information at night and regardless of cloud cover, whereas optical methods highly depend on daylight and good climatic conditions. Optical and thermal acquisitions provide DEMs using stereo-photogrammetry (Diefenbach et al., 2012, 2013 ; Bagnardi et al., 2016 ; Carrara et al., 2019), and eventually velocity maps and strain maps resulting from image correlation (Walter et al., 2011 & 2013). Radar imagery enables the quantification of the thickness and volume of domes and their associated flows emplaced at the surface, using either the amplitude (Wadge et al., 2011 ; Walter et al., 2015 ; Arnold et al., 2017 ; Angarita et al. 2022) or the phase (e.g Kubanek et al., 2017 ; Ordonez et al., 2022) acquired from bistatic interferometry (two images acquired simultaneously). Retrieving the surface topography from the phase of monostatic radar data (one image acquired per measurement) requires the analysis of a long time series in order to separate elevation changes from surface deformation and atmospheric artifacts. Moreover, monostatic radar is also not appropriate for dome studies due to loss of coherence on short timescales (Wang et al., 2015). Therefore, bistatic radar data are favored and ensure a better accuracy when available (Bato et al., 2016). Bistatic data have the additional advantage of being unaffected by coherence loss due to changes in surface properties, and this coherence loss strongly reduces the use of the phase of radar

data acquired at different times (Salzer et al., 2016). However, some studies succeeded in imaging changes in the summit areas of volcanoes using monostatic SAR data (Richter et al., 2013).

Instruments to monitor volcanoes are either ground-based or remote, and episodic or permanent, depending on the spatial and temporal resolution required, as well as the operating budget available. Multi-sensor studies are often carried out to estimate volumes (Ryan et al., 2010). Studies from the past century were mainly tracking the topography of domes using ground-based leveling, photographs and theodolites. Ground-based optical and/or thermal cameras have also been widely used to track dome topography, like on Mt St Helens, USA (Major et al., 2009), on Volcán de Colima, Mexico (Walter et al., 2013), or on Merapi, Indonesia (Hort et al., 2006 ; Ratdomopurbo et al., 2013 ; Kelfoun et al., 2021). Ground-based radar observations associated with seismicity also provided insights on lava dome growth, such as at Soufrière Hills volcano, Montserrat (Wadge et al., 2008 ; Ryan et al., 2010). However, due to steep-slopes and explosions, it can be difficult to implement ground-based measurements close to the crater for visibility, accessibility and security reasons (Darmawan et al., 2018). In contrast, remote-sensing using instruments mounted on helicopters, airplanes, more recently on unmanned aerial vehicles (UAVs), or satellites has the ability to provide cost-effective quantitative information on the crater area with minimized risk and spatially continuous coverage (Zorn et al., 2019 & 2020). Generally, an increase in the distance at which the measurement is made results in an increase in the area covered at the cost of a decrease in spatial resolution and accuracy.

Airborne instruments have been successfully used to produce DEMs of hazardous lava domes: examples include helicopter kinematic laser on the Soufrière Hills dome, Montserrat (Sparks et al., 1998), low-cost helicopter cameras above Mount St Helens, USA (Diefenbach et al., 2012), UAVs optical images on the Merapi dome in 2012-2015 (Darmawan et al., 2018), or thermal infrared imagery of the Volcán de Colima dome, Mexico (Thiele et al., 2017 ; Salzer et al., 2017). Thermal infrared imagery can also be used to infer the effusion rate using equations linking temperature, heat loss, and crystallization of lava. This technique was in particular applied to MODIS data during the dome growth episode of 2006 at Merapi volcano (Harris et Ripepe, 2007 ; Carr et al. 2016).

Airborne monitoring is, however, inconsistent, weather-dependent and costly, which led to an increase in the use of satellite imagery in recent years. The huge amount and diversity of remote-sensing data from various space agencies provide more continuous data with regular revisit times. These data are sometimes open source (Sentinel-1 for radar and Landsat-8 or Sentinel-2 for optic). Numerous automated processing chains are implemented in observatories, sometimes using deep learning algorithms, thus increasing the rapid response to a volcanic crisis and eventually providing an insight into the probability of an eruption (Anantrasirichai et al., 2019 ; Milillo et al., 2021). Automated chains usually provide ground displacement time series from InSAR and GNSS, sometimes even amplitude and coherence time series (d'Oreye et al., 2021). However the monitoring of summit domes, which are typically a few hundred meters wide, still requires high resolution satellite data, such as TanDEM-X (bistatic radar imagery) (Zink et al., 2014), COSMO-SkyMed (monostatic radar imagery) or Pléiades (stereo optical imagery). These data are not routinely acquired and are only tasked based on specific requests through scientific proposals, for volcanoes labeled as Supersite by the Committee on Earth Observation Satellites (CEOS) for example. Some initiatives such as the International Charter Space and Major Disasters Activation Map or the French Cellule d'Intervention d'Expertise Scientifique et Technique (CIEST2) (Gouhier et al., 2022) are also meant to favor acquisitions in case of volcanic crises.

Despite their high potential for summit dome monitoring, TanDEM-X DEMs have so far mainly been used to track lava flows on relatively flat terrain (Kubanek et al., 2017 ; Poland, 2014 ; Rowland et al., 2003 ; Ebmeier et al., 2012 ; Lundgren et al., 2019) or volcanic edifice slopes (Albino et al., 2015 ;

Bato et al., 2016 ; Carrara et al., 2019 ; Arnold et al., 2016), PDCs (Albino et al., 2020) or large scale crater shape evolution (Kubanek et al., 2015). Pléiades DEMs have been widely used to track lava flows (Bagnardi et al., 2016 ; Pedersen et al., in revision ; Gouhier et al., 2022), PDCs and dome growth (Moussallam et al., 2021) and major events of dome destruction (Carrara, et al. 2019). To our knowledge no Pléiades and TanDEM-X images have been used jointly to produce DEM time series of lava domes on dome building volcanoes, despite the high potential benefits to the volcanological community, both in terms of monitoring domes and modeling their behavior. Indeed, the joint use offers the possibility to quickly produce high resolution DEMs to follow the morphological evolution of domes over time, and to easily combine the two datasets as they are consistent with each other: for example, if cloud cover prevents optical acquisition, radar images can help cover this data gap. The combination of the two datasets therefore allows for better spatial and temporal resolution, the only remaining limitations being the cost and potential latency of delivery of TanDEM-X and Pleiades data. These data could avoid the use of drones in difficult climatic conditions. They could be used in conjunction with DEMs generated by SAR shadows, providing even better temporal resolution for monitoring purposes. However, the potential of TanDEM-X and Pleiades for monitoring small volume changes (less than 1 Mm^3) remains to be clarified, which is one of the objectives of this study.

In this study, we focus on the spatial-temporal evolution of a lava dome that appeared on 11 August 2018 at Merapi volcano, Indonesia. We take advantage of the high spatial resolution of optical Pléiades images and radar TanDEM-X data to build a total of twenty DEMs with a horizontal resolution of 3 m and a vertical accuracy of a few meters over a period from 10 July 2018 to 09 December 2019. Topographic changes with respect to a reference DEM from 2013, manual dome outline mapping, and volume estimates are derived from these DEMs, enabling a better understanding of the dome evolution over one year. Volume estimates derived from satellite imagery are compared to independent volume estimates from in situ drone measurements and the ability of both datasets to quantitatively track the evolution of the dome is discussed.

2. Merapi volcano recent activity and monitoring devices

Located about 30 km north of the city of Yogyakarta near the south coast of Java island (**Fig. 1**), Merapi is an extremely hazardous dome building stratovolcano, with about 2 million people living less than 30 km away from the almost permanently active crater. The volcanic activity at Merapi started more than 100,000 years ago, and the construction of the recent Merapi cone initiated around 4,800 years ago (Gertisser et al., 2012). The recent period is characterized by cyclic effusive growth of viscous lava domes, followed by their partial or total destruction (Camus et al., 2000 ; Ogburn et al., 2015). Dome are frequently destroyed by gravitational collapses (VEI 2) every 4-5 years (Voight et al., 2000a ; Newhall et al. 2000 ; Pallister et al. 2013), resulting in pyroclastic density currents (PDCs) driven downhill at high velocities and frequently reaching 7 km long distances (Abdurachman et al., 2000). During rainy seasons, PDCs can be remobilized forming lahars, thus increasing casualties (Lavigne et al., 2000). Less frequent (every 50-100 years) explosions of relatively high intensity (VEI 3-4) can cause dome destruction and generate major PDCs that can reach up to 17 km from the summit (Komorowski et al., 2013).

The last major explosive eruption (VEI 3-4) occurred in November 2010, resulting in a horseshoe-shaped crater of 400 m wide and 250 m deep. When the eruption ended, it resulted in a lava dome of 150 m wide and 40 m high, shaped like a plateau (Darmawan et al., 2018). The crater is opened to the south-east in the direction of Gendol gorge (Kubanek et al., 2015). This new crater morphology offers direct visibility to the inside of the crater for optical cameras (Kelfoun et al., 2021).

The 2018 dome extruded from the middle of a pre-existing fissure on the plateau, after six successive explosions between 2012-2014 (Kelfoun et al., 2021 ; Darmawan et al., 2018). The first UAV picture was acquired on 12 August 2018. The new dome was emplaced at the same location as the prior phreatic vents, with a 47 m long oval shape, having a width of 17 m and a height of 2 m. This black lava dome had a blocky structure (carapace), an andesitic to andesite-basaltic composition, and a temperature over 100°C.

Merapi is closely monitored by the BPPTKG (Volcano Research and Technology Development Center), which is part of the CVGHM (Indonesian Geological Agency's Center for Volcanology and Geologic Hazard Mitigation), in Yogyakarta, with ground-based, airborne and spaceborne tools. Currently, a Global Positioning System (GPS) network is implemented around the volcano (Beauducel, 1999), although quite far from the summit area (closest station PASB, ~650 m from crater), as well as an Electronic Distance Measurements (EDM) array. Several remote-sensing datasets provide various information on the ground deformation of the volcano in near-real time as they are processed following an automated chain: open source Sentinel-1 provide interferograms every six to twelve days (Pinel et al., 2021), Sentinel-2 optical images provide a view of the summit area, and B12 band thermal imagery provide frequent maps of thermal anomalies. These data are gathered in the WEBOBS platform (Beauducel et al., 2020). During the 2018 dome growth, in situ drone measurements were carried out using a low-cost UAV Quadcopter model to obtain detailed morphological data of the summit with a resolution of 0.5 m (Granados-Bolaños et al., 2021) and an accuracy of 40 cm. The aerial photography of Merapi was done using DJI Phantom 4 PRO, a Quadcopter with a payload of less than 1.3 kg, with a very stable flight controller, a sensitive gimbal, and a high-quality camera (20 megapixels camera, 4 K video capable). The flight execution was carried out at a height of 350 m over the summit with a mapping flight speed of 15 $m.s^{-1}$ (**Fig 1.C**) and 80% overlap. Each aerial photo is georeferenced, with dimensions of 4864 x 3648 pixels, with a horizontal resolution of 72 dpi.

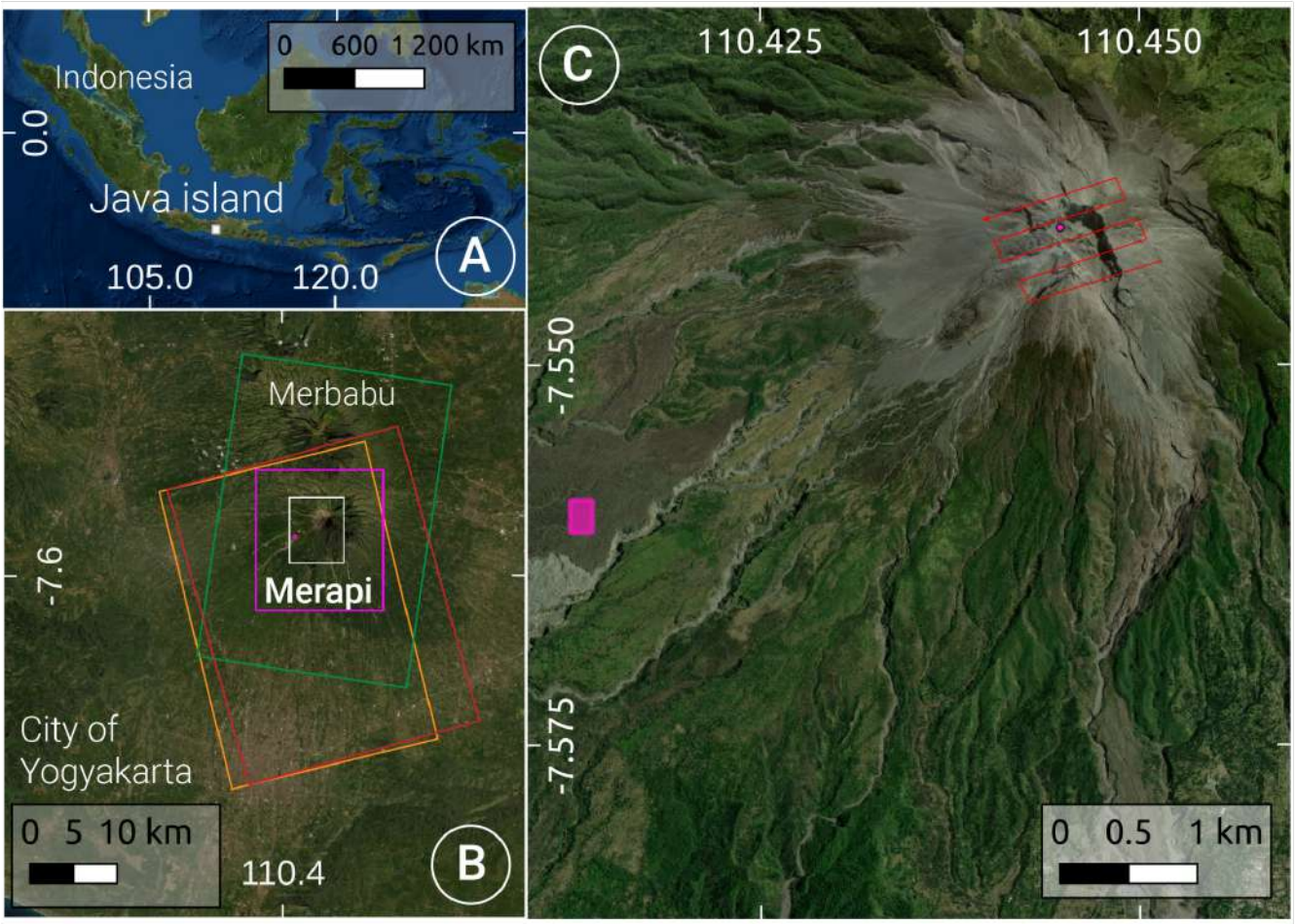

Figure 1. Geographical setting of Merapi volcano, Indonesia (Google Earth views). Panel A: location of the volcano (white square), near the south coast of Java island, part of a volcanic arc resulting from the subduction of the Australian plate beneath the Sonde plate. **Panel B**: Merapi volcano is surrounded by the Merbabu volcano to the north, by plains and crops to the west, the Indian ocean to the south and the Kedu plain to the east. It is only 25 km to the north of the city of Yogyakarta. The footprint of TanDEM-X and Pléiades satellites used in this study are displayed, respectively TanDEM-X descending track 134 (green rectangle), ascending track 96 (orange rectangle) and track 20 (red rectangle), and Pléiades (pink rectangle). The white rectangle covers the area of Panel C. **Panel C**: Zoom on Merapi: vegetation stops around 2300 meters a.s.l, the volcano is covered by ash up to the summit horseshoe shaped crater inherited from the 2010 eruption. The crater is connected to the southeast to the Gendol valley. At the summit, slopes reach on average 40°. The flight path of the drone is along the red line with the location of the take-off/landing site and the start and end location of aerial acquisitions. The pink dot in the crater corresponds to the seeding point location of the unwrapping and the pink box on the southwest flank shows the area for phase referencing for TanDEM-X DEMs (See Material and Methods).

3. Material and Methods

3.1. High resolution optical images: Pléiades data

3.1.1. Data description

The Pléiades satellites acquire stereo or tri-stereo images in Panchromatic mode over the same area during a single-pass (Gleyzes et al., 2012). The parameter B (maximum baseline between 2 stereo-images) over H (height of satellite, assumed constant ~700 km) characterizes the geometry of acquisition and influences the quality of the photogrammetric reconstitution. A B/H ratio superior to 0.25 is optimum for processing DEMs, depending on the relief (see B/H ratio description in Pléiades User Guide). In this study, the B/H ratio was retrieved from the code howstereo.py (Copyright (C) 2020 Arthur Delorme), using incidence angles across and along track as well as azimuth, available in the metadata. Here we use and process one stereo pair of Pléiades optical images acquired in April 2013, to derive a reference DEM, and five tri-stereo Pléiades optical images (fifteen panchromatics) acquired between February and September 2019. The reference DEM characterizes the summit topography before the initiation of the dome growth. Pléiades panchromatic images have a nominal resolution of 0.5 m. Geometrical characteristics and dates of acquisition of the six images used are given in **Table 1**.

3.1.2 Processing method with Ames Stereo Pipeline (ASP)

Pléiades images were processed using Ames Stereo Pipeline (ASP), an open source suite dedicated to stereophotogrammetry, developed by NASA (Shean et al., 2016). Each image of a given stereo couple or triplet was first projected on a preexisting SRTM 2000 (Shuttle Radar Topography Mission) DEM of 30 m ground pixel size (**Fig 2.A**). Then, a point cloud was generated using pixel correlation and triangulation between the two or three images. Finally, a 3 m pixel size DEM was derived from this point cloud. As no ground control points were used, the absolute positioning of the DEM produced was not fully accurate. The six DEMs produced were coregistered in order to align and minimize positional biases between the successive DEMs following the methodology described in Berthier et al. (2007). Small gaps in data due to clouds of limited size over the summit area were interpolated during the post-processing from five neighboring pixels using an inverse distance weighting function of QGIS. Note that in addition to the DEMs produced, the ortho-images obtained are useful to identify surface changes induced by the eruptive activity.

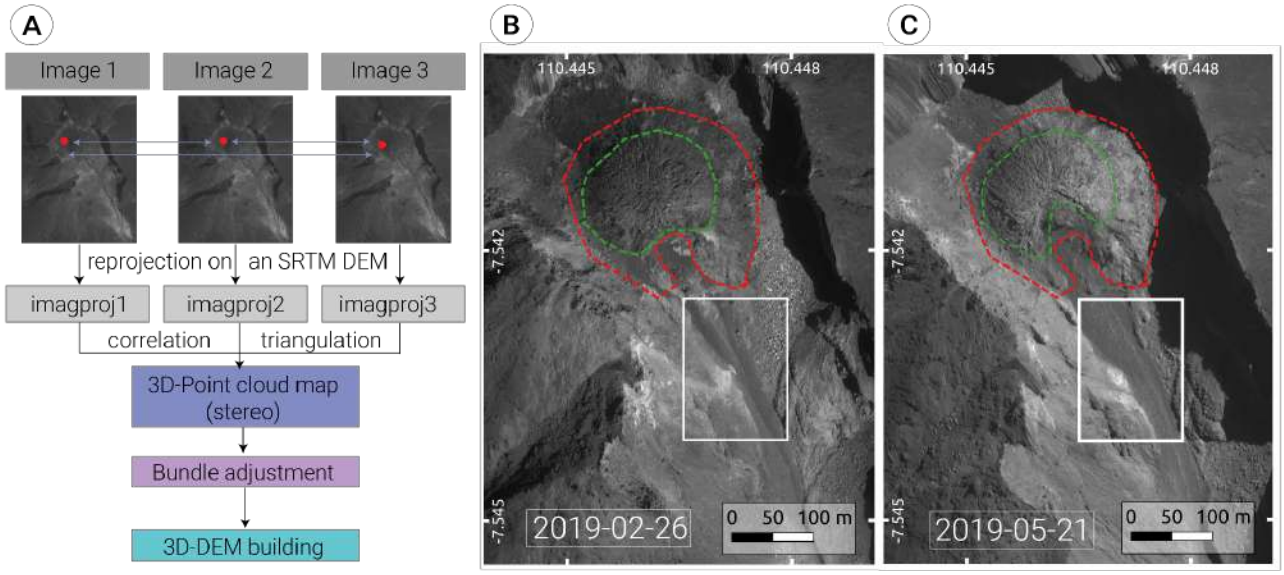

Figure 2. Pléiades images workflow with ASP and optical panchromatic ortho-images. Panel A: Correlation (gray arrows) between pixels (red dots) produces a stereo map from three images acquired

with a slightly different geometry. This point cloud is then georeferenced using bundle adjustment, a method which refines the pixel coordinates by minimizing the errors between observed and predicted pixel position. **Panel B:** Panchromatic image from 26 February 2019 projected on a SRTM DEM. The extent of the dome is trackable thanks to grayscale contrast between old material (light gray) and new emplaced material (dark gray). From this contrast we can estimate a first order outline for the 2018 dome (dotted red outline). Within this extent, a rougher radial surface stands out (dotted green outline). **Panel C:** Panchromatic image from 21 May 2019 projected on a SRTM DEM. Two main differences compared to the previous 26 February 2019 image are trackable in the summit area: the southern part of the dome is partially destroyed (green outline) and new material was emplaced to the southeast (white outline).

3.2. High resolution radar images:Tandem-X data

3.2.1. Data description

The TanDEM-X satellite mission (Zink et al., 2014) is aimed at building high precision DEMs every eleven days, relying on the physics of radar waves interferometry in bistatic mode. During one "single-pass" acquisition, two nearly identical SAR sensors aboard the TerraSAR-X and TanDEM-X satellites fly in close helical formation (Krieger et al., 2007), resulting in two X-band radar images acquired simultaneously over the same area. In this case, the phase difference between the two radar images is an interferogram that corresponds only to the contribution of the topography (reference and residual topography), thus bypassing the atmospheric and deformation contribution to the phase, due to simultaneous acquisitions (Kubanek et al., 2015) (**See Supplementary material for further details**). From the phase change in radians, the terrain elevation h can be retrieved in meters using the slant-to-height conversion (Yoon et al., 2009):

$$h = -(\lambda * r * \sin(\theta) * \phi_{\mathrm{InSAR}}) / (4\pi B_{\perp}) \quad (1)$$

where λ is the X-band wavelength (roughly 0.031 m), r the geometric range distance of the ground to the master satellite, θ the incidence angle with respect to the vertical, and $B_{\perp}$ the effective perpendicular baseline between the two satellites, which is in the case of bistatic mode half of the perpendicular component of the distance between the two satellites (Kubanek et al., 2021). The sensitivity of the phase to elevation changes can also be expressed in terms of the height of ambiguity (*ha*), defined as the height difference corresponding to a phase shift of 2π. The larger the $B_{\perp}$, the smaller the *ha*, meaning that the measurement will be sensitive to smaller changes in elevation. However, this may make unwrapping more difficult because there is a higher fringe gradient.

The summit area of Merapi volcano is imaged by three different tracks of TanDEM-X: the descending track D134, the ascending track A96 and the ascending track A20 (see **Table 1** for the characteristics of all images processed in this study, see **Fig 1.B** for the footprints). Comparison between three tracks enables selecting the tracks with best visibility on the crater area. Coherence and amplitude images are shown for each track for images acquired in June 2019 in **Fig. 3**. Images are displayed in radar geometry : depending on the track, images are not oriented and distorted the same way. Descending track images (column A) are horizontally mirrored compared to the terrain geometry, meaning the image is reversed along the west-east direction. Inversely, ascending track images (column B and C) are vertically mirrored compared to the terrain geometry, meaning the image is reversed along the north-south direction. Because of a higher angle of incidence, which greatly reduces the effects of

layover and foreshortening, the ascending A96 gives the best view of the dome, even if shadow effects induced by the crater walls limit the visibility of the western part of the dome and in the Gendol valley located below the dome. Based on this observation, we focused our study on the use of sixteen TanDEM-X images from the ascending track A96.

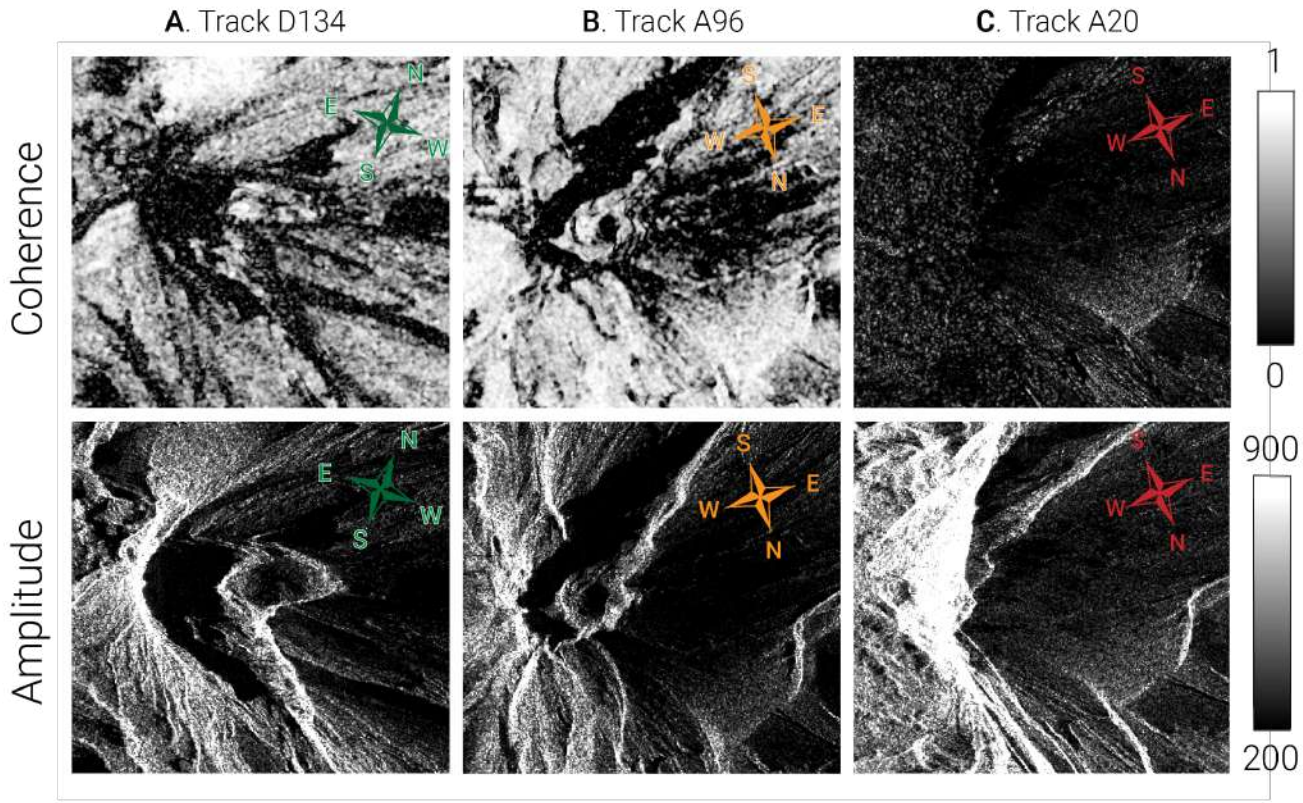

Figure 3. Amplitude and coherence images for the three TanDEM-X tracks available over Merapi volcano summit area. Panel A: Descending image from track D134 acquired on 18 June 2019. The dome is strongly distorted, with a shadow zone on its Western part and low coherence. **Panel B**: Ascending image from track A96 acquired on 16 June 2019. The dome is less distorted than on D134, although shadowing occurs on the eastern flank of the dome. Coherence is relatively high on the dome except on the shadow area. **Panel C**: Ascending image from track A20 acquired on 11 June 2019. The dome is not visible at all due to major foreshortening.

Date	Orbit	Track number	Effective ha (m)	Lava dome volume (Mm³)
2018/07/10	Ascending	96	84.39	0.052
2018/08/12	Ascending	96	109.83	0.055
2018/08/23	Ascending	96	120.19	0.10
2018/09/03	Ascending	96	131.49	0.12
2018/10/17	Ascending	96	168.1	0.26
2018/11/21	Descending	134	23.37	
2018/11/30	Ascending	96	38.4	
2019/03/09	Ascending	96	83.62	0.66
2019/03/31	Ascending	96	94.59	0.59
2019/04/11	Ascending	96	100.96	0.56
2019/04/22	Ascending	96	42.87	0.66
2019/04/24	Descending	134	26.49	
2019/06/05	Ascending	96	47.53	0.64
2019/06/11	Ascending	20	21.18	
2019/06/16	Ascending	96	48.94	0.66
2019/06/18	Descending	134	30.54	
2019/06/22	Ascending	20	21.74	
2019/06/27	Ascending	96	50.19	0.66
2019/06/29	Descending	134	31.13	
2019/07/03	Ascending	20	22.48	
2019/07/08	Ascending	96	51.67	0.68
2019/09/14	Descending	134	33.14	
2019/09/25	Descending	134	34.48	
2019/11/28	Ascending	96	74.68	0.53
2019/12/09	Ascending	96	85.42	0.50

Date	B/H	Along track incidence(°)	Across track incidence(°)	Lava dome volume (Mom3)
2013/04/26	0.20			
03:08:25		-8.817217220395586	-6.898799157153648	
03:08:43		2.383020158158021	-9.223405423996606	
2019/02/26	0.58			0.65
03:07:59		-20.09433944147328	-4.996002238992582	
03:08:35		1.557682621504057	-9.617006567140558	
03:08:53		11.90792550774587	-11.78130916077721	
2019/05/21	0.64			0.61
03:11:26		-21.11026123928664	-13.48404049447741	
03:12:04		1.188814345094415	-17.93289482389636	
03:12:26		14.49136020831147	-20.53711324954333	
2019/06/18	0.52			0.66
02:56:49		-8.533043237688107	20.69034026318977	
02:56:59		-2.574938590384239	19.52180668358012	
02:57:38		20.41997423763934	14.84033163022764	
2019/08/21	0.60			0.63
03:05:42		-17.83986894461046	3.576958740279529	
03:04:45		-4.414469766169287	0.5951481585683186	
03:05:08		15.75972447437973	-3.826905908328997	
2019/09/09	0.42			0.63
03:08:39		-12.55068782653866	-6.984662271092217	
03:09:17		-5.472328159858717	-8.482084153786536	
03:08:51		9.790743438505295	-11.65541947384622	

Table 1. TanDEM-X and Pléiades data along with their main characteristics. Top: TanDEM-X data in Stripmap acquisition mode and heights of ambiguity. Volume estimates were calculated only for dates in bold for track A96, using an outline derived from the produced DEMs (referred to as RS outline later in the paper, See Fig 6). **Bottom**: Pléiades B/H ratio and across/along track incidence angle for each tri-stereo pair and the time of acquisition. Please note the reference stereo-pair of 26 April 2013 was used for the radar reference DEM simulation and for the differencing of each DEM. Volumes are calculated the same way as volumes from TanDEM-X.

3.2.2. Processing method

TanDEM-X images were processed with an adapted workflow relying on ROI_PAC (Rosen et al, 2004) and developed at ISTerre, Grenoble (**Fig 4.A**). For each date, we obtained interferograms corresponding to the residual topography with respect to the reference topography. The quality of the interferogram in the small dome area strongly depends on the choice of the reference DEM. Here, we

used a reference DEM resulting from the merging of a large-scale SRTM 30 m DEM oversampled to 3 m and a 3 m resolution DEM of the summit area, derived from stereo Pléiades images acquired in April 2013.

The 2013 DEM is suited as a pre-eruptive dome DEM, because between 2010 and 2018, only a series of phreatic eruptions occurred in 2014 without major morphological changes, except a minor wall destabilization in the south-eastern flank.

The resulting interferogram (**Fig 4. C**) is then filtered (Goldstein and Werner, 1998 , **Fig4.D**), unwrapped (Chen and Zebker, 2001, **Fig 4.E**), and referenced with respect to a stable area (**Fig 4.F and Fig 1.C**). Slant-to-height conversion is then performed using equation (1). Ultimately, interferograms are geocoded from radar to ground geometry, with a look-up table.

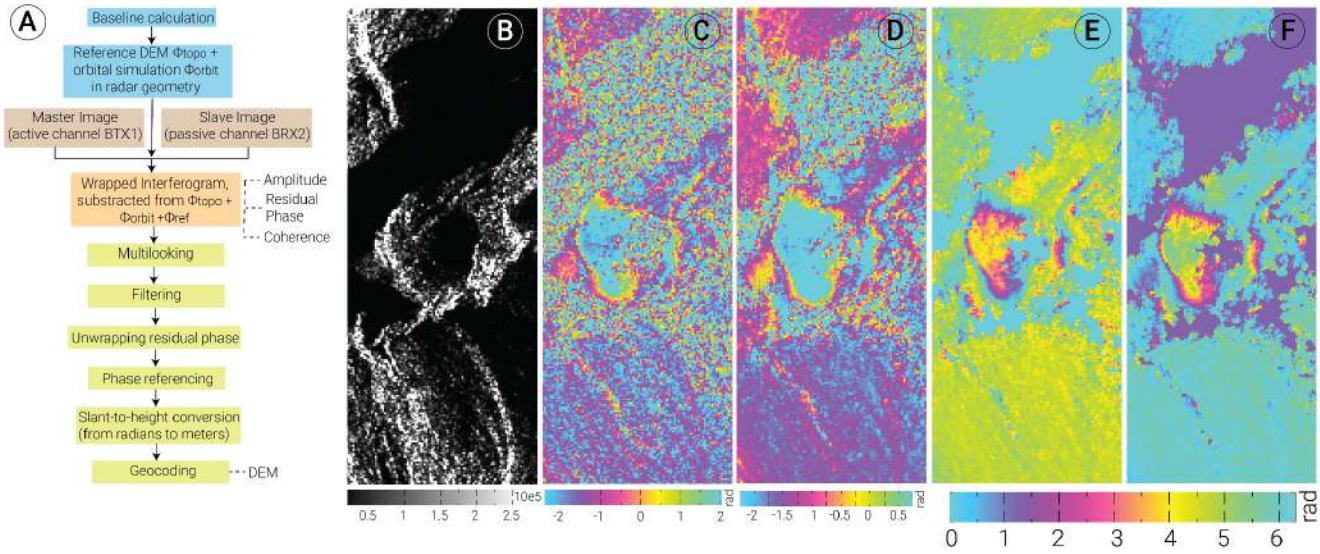

Figure 4. **General workflow used to generate TanDEM-X DEMs. Panel A:** The adapted processing chain starting from the images in .slc ROI_PAC format. After wrapped interferogram production, post-processing steps allow for filtering good coherence pixels (above 0.4), unwrapping, referencing, geocoding and eventual shift corrections for vertical misalignment. **Panel B**: Zoom on the radial dome in the 22 April 2019 amplitude image. Shadowing occurs on the eastern side of the dome due to its height and the satellite viewing angle. **Panel C:** Zoom on the dome in the corresponding wrapped interferogram. Note the noisy random distribution of the phase in corresponding shadowed areas on the amplitude image. Signal is present on the dome. **Panel D:** Zoom on the dome in the filtered wrapped interferogram. Only pixels with a coherence above 0.4 are conserved. Note that the outline of the topographic fringes is different from Panel C because the scale is different. **Panel E:** Zoom on the dome in the filtered and unwrapped interferogram. Unwrapping succeeded in areas of good coherence and with sufficient signal. The dome has been successfully unwrapped, but notice the surrounding areas where no topographic change is expected are not equal to 0. **Panel F**: Zoom on the same area as Panel E with a shift correction from a reference area without topographic changes, resulting in areas outside of the dome being equal to 0.

In addition to the DEMs directly derived from the interferograms, we also produced amplitude and coherence images, and used the latter to build vertical precision maps. As the track is ascending, amplitude and coherence maps show shadowing on the eastern slopes of the volcanic edifice. SAR amplitudes are a useful tool to assess dome shape, surface roughness and eventually highlight the emplacement of new lava at the surface. False color amplitude maps were thus computed between two

dates in order to better evidence changes in the surface properties and shape (Solikhin et al., 2015; Walter et al., 2015) (**See Text S1 Supplementary material for further details**). Coherence maps reflect the spatial stability of the pixels between two radar images. A good coherence (value close to 1) means the pixels are highly stable and thus the topography derived from the phase is accurate. Within the dome, the average coherence is 0.44 due to shadowing. When masking the dome with coherence values below 0.6, to exclude shadowed zones, the average coherence reaches 0.83.

3.3. Elevation change maps uncertainties

We computed the mean and standard deviation of each elevation change map on stable areas out of the summit to correct for eventual vertical shifts (**See Text S2 and Table S1 in Supplementary material for further details**). For Pléiades DEMs, we added a filter on slopes which excluded slopes above 70°. For TanDEM-X DEMs, we added a filter on coherence as areas with good coherence (above 0.8) have more spatially stable pixels and are expected to be characterized by a lower uncertainty in the retrieved elevation than areas of low coherence (below 0.4) (**Fig 5.B**) (**see Table S1 and Fig S1 in Supplementary material for further description of the selected pixels**). We corrected the fifteen TanDEM-X DEMs by subtracting the mean of the non-deformed areas of good coherence from the whole DEM. For both TanDEM-X (**Fig 5.A**) and Pléiades (**Fig 5.C**), we observe a gaussian distribution of the elevation difference, even though on some TanDEM-X we observe a small asymmetry. It seems the smaller the *ha*, the more the curve is asymmetric (smaller standard deviation but also smaller number of pixels centered around 0 value).

There is a positive linear relation between standard deviation and height of ambiguity *ha* (**Fig 5.B**). As a consequence, DEMs derived from pairs characterized by a large *ha* show higher artifacts outside the crater than the ones obtained with a smaller *ha*. Moreover, coherence also impacts the standard deviation of non deformed areas (**Fig 7.B**) : in the case of bad coherence areas, mean (green dot) and standard deviation (green error bars) are higher than in the case of good coherence (blue dots and error bars). This leads us to use the precision maps σ(z) (**Fig 5.D**), functions of coherence γ and *ha* , as a proxy for vertical uncertainties on the dome, for TanDEM-X derived DEMs (**See Text S2 in Supplementary material for further details**):

$$\sigma(z) = \frac{\sqrt{\square}}{\square} \quad (2)$$

The precision maps allow us to assess vertical precision of height estimates for each pixel of the DEMs. Precision maps display the spatial variability of the vertical accuracy of heights on the dome, with bad precision over the shadowed area and good precision on the rest of the dome : for large *ha* and low coherence, the value of precision is high, meaning accuracy is low, and inversely. Mean vertical precision over the dome of coherence values above 0.8 is 14 m (± 8 m), with best precision obtained for DEMs of small height of ambiguities: precision of 5 m is predicted for an effective height of ambiguity of about 50 m. For Pléiades, uncertainties are estimated using classic standard deviation estimated from non deformed areas and are around 7 m on average (**Fig 5.C and Table S1**).

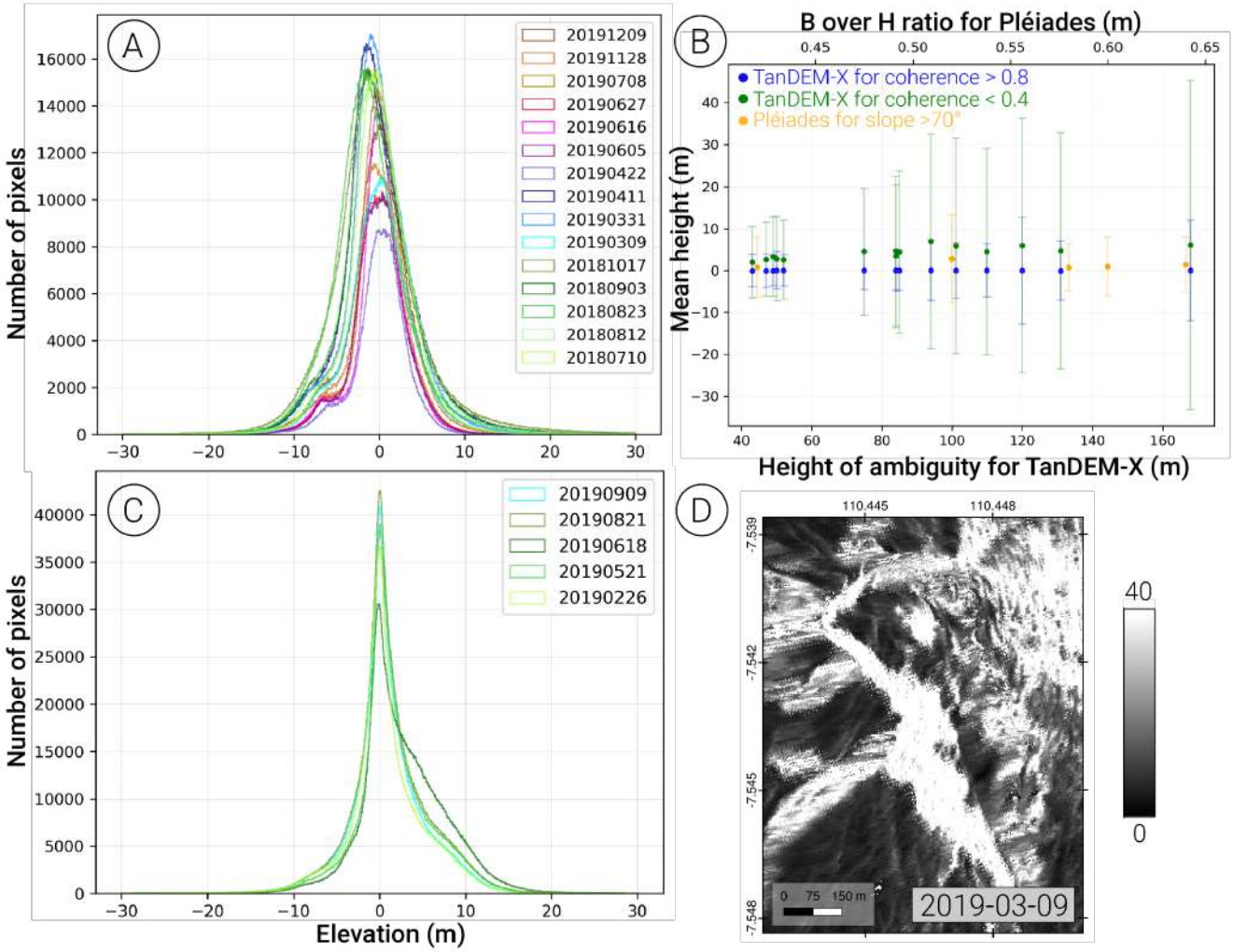

Figure 5. **Standard deviation and mean for elevation change maps derived from TanDEM-X DEMs and Pléiades DEMs for areas with no topographic changes compared to 2013**. For TanDEM-X DEMs, we applied a specific threshold on the coherence and for Pléiades a specific threshold on slopes. **Panel A**: histogram for TanDEM-X DEMs corrected from their vertical offset, considering coherence above 0.8 (good coherence). As a consequence from the vertical offset correction, the mean is centered around 0 and standard deviation does not exceed 20 m. **Panel B**: mean of non-deforming areas as a function of the effective height of ambiguity for TanDEM-X, for good (blue) and bad (green) coherence areas, and as a function of B over H ratio for Pléiades (orange). **Panel C**: histogram for Pléiades DEMs, considering an additional filter excluding slopes above 70° where big outliers can be expected. The mean is centered on 0, showing that the vertical offset estimated, when coregistering the various DEMs, has been successful. **Panel D**: Precision map of 09 March 2019 showing the spatial variability of the vertical precision on the dome, with bad precision over the shadow area and good precision of about 5 m at best on the rest of the dome.

3.4. Volume estimation

From the elevation change maps, we retrieve the volume of the dome for each date. The outline of the dome is defined in two ways for comparison purposes between the various datasets. A first outline of the dome is derived from the area selected for drone measurements by the BPPTKG (referred to as BPPTKG dome outline in the rest of the paper, surface area of 18177 m^2) in order to compare our

volume estimates from Pléiades and TanDEM-X to their estimates from drone using the same surface of the dome. A second outline is manually traced using the elevation change gradient on produced DEMs (referred to as Remote Sensing RS dome outline, surface area of 27509 m^2) : we consider this outline as a more relevant outline with respect to our dataset, allowing us to include the north-western part of the dome, and thus derive proper volume estimates from our observations. Then, the average height within this surface is computed for positive values on DEM differences and finally the average lava volume is calculated. Ultimately, an average magma discharge rate can be estimated by considering the time derivation. Please note that excluding negative values does not mean excluding negative changes of topography within the dome : negative values are negative with respect to the reference DEM of 2013, therefore we consider them as outliers, confirmed by the fact that there are very few of them and they are sparsely distributed. A loss of topography of the dome, with respect to 2013, still corresponds to a positive value.

More precisely, during the dome growth and the so-called "steady" period, we do not measure negative changes, but it does not mean loss of topography did not occur. Indeed, as described in Darmawan et al., 2020, ground-based optical cameras show scars and destabilizations on the edges of the dome, but we can not detect them on our time series : either they are not well resolved in our DEMs, or they are transient and thus balanced by lava supply maintaining "constant" topography of the dome between 2 satellite acquisitions. In addition, we want to mention that significant negative changes were observed by the end of 2019 when explosions occurred and partly destroyed the dome, as displayed in cross-sections (**Fig. 10**) and volumes (**Fig. 12**).

The volumes derived from the twenty DEMs, using the first BPPTKG outline of the dome, are then compared to the volumes calculated by the BPPTKG from their own drone measurements. We also performed volume calculation of the accumulation zone below the dome only in Pléiades DEMs, in a similar way, with our own outline only.

Uncertainties in the volume were estimated using the standard deviation of the height within the dome outline multiplied by the surface of the dome. We also added a component corresponding to the uncertainty of the outline itself by estimating the volume on a section around the dome outline of one more pixel of 3 m. For the volume uncertainties from the drone, we consider the accuracy of 40 cm multiplied by the surface of the dome.

4. Results

Based on the dome monitoring performed by drone measurements, and following the description of Kelfoun et al., 2021, we discriminate three main stages in the dome evolution between 2018 and 2019. The first stage is a spatial expansion within the crater from August to December 2018. This "growth stage" is followed by a "steady stage" of constant elevation and shape of the dome within the crater. This constant elevation is due to new lava effusion with compensative gravitational collapse into the Gendol valley from January to September 2019, followed by a final stage with partial destruction of the dome until June 2020. The first image of our dataset also provides information on the crater before the dome appeared. Based on the information provided by the thermal cameras (Kelfoun et al., 2021), we consider that the growth of the dome is mainly exogenous, but we cannot totally exclude that some material is emplaced beneath or inside the dome.

We first present the Pléiades panchromatic images, only available during the "steady stage" period, and associated derived DEMs. These data provide quantitative information on the shape and topography of the dome, as well as complementary information on the Gendol valley below. Then we present TanDEM-X results as they provide more information on the chronological evolution of the dome,

especially the early growth and the later start of destruction in favor of explosions. The comparison of the two datasets is carried out over the "steady stage" period when both datasets are available and then used to estimate lava volumes and emission rates.

4.1. Pléiades imagery: "steady stage" period

The analysis of the five Pléiades panchromatic tri-stereo acquisitions provides information on the 2018 dome after emplacement (**Fig 2.B and C**). Within the horseshoe shaped crater, the extent of the dome is trackable thanks to grayscale contrast between old material (light gray) and new emplaced material (dark gray). From this contrast we estimate the 2018 dome is ~200 m diameter. Within this extent, a rougher radial and cracked surface stands out. The image of 21 May 2019 shows two main differences compared to the previous image of 26 February 2019 : the southern part of the dome is partially destroyed and some new and thin coarse material has deposited to the southeast. The following images show no major changes in the summit area.

No significant elevation changes in the dome are recorded between February and September 2019, corresponding to the "steady stage" in the evolution of the dome: the maximum dome thickness is ~ 40 meters and cross-sections evidence the dome is limited by steep slopes (**Fig 6 A, B and profile AA' in Fig. 6C**). The shape of the dome is radial with an extension to the northwest (**Fig 6.A**), which is consistent with the panchromatic images. Pléiades also provides additional information on the southeastern Gendol valley below the dome. Successive Pléiades-derived DEMs reveal increasing topography in the 400 m below channelized in the gorge (**Fig 6**). The maximum elevation goes from about 5 meters in February 2019 up to 15 meters in September 2019, as displayed on the west-east cross-sections of the accumulation area (Profile BB' in **Fig 6.C**).

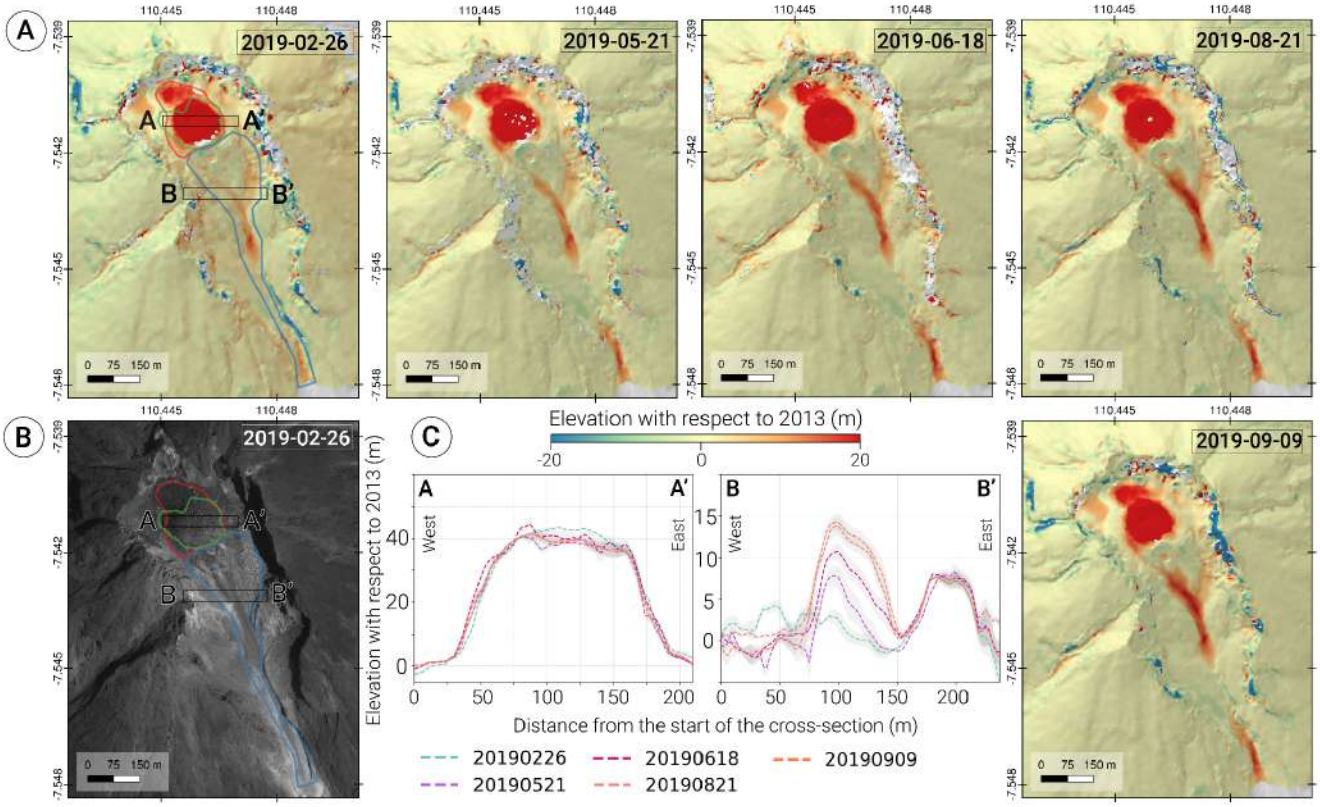

Figure 6. Pléiades DEMs and cross-sections along the dome and north of the accumulation zone. **Panel A:** successive Pléiades DEMs showing the dome with no significant change in elevation and shape. On the contrary, the accumulation zone below increases in elevation. **Panel B:** outlines of the dome and the accumulation zone on the Panchromatic image of Pléiades of 26 February 2019. The red outline corresponds to the outline derived from the DEMs in this study (Remote Sensing RS outline), the green outline corresponds to the delimitation of the surface monitored by drone flights (BPPTKG outline) and the blue outline corresponds to the accumulation zone. Cross-sections along the west-east profile are done using the mean of elevation within a ten pixels wide window (see rectangles displayed on the first DEM), and considering the mean precision along the cross-sections as an estimate of the uncertainties. **Panel C:** West-east (A-A') cross section across the dome and west-east (B-B') cross-section along the top of the accumulation zone for the five dates of Pléiades images. Light gray area corresponds to standard deviation. Note the difference in scale for heights.

4.2. TanDEM-X dataset: temporal evolution

4.2.1. Before dome emplacement

Amplitude maps clearly display the horse-shoe shaped crater area of ~ 400 m wide leading to the Gendol gorge to the south-east. The first amplitude map from 10 July 2018, prior to the appearance of the dome, reveals in the middle of the crater a northwest-southeast oriented shadow crossing the whole plateau (**Fig 7B)**. We interpret this linear shadow as the fracture described in Kelfoun et al., 2021. It is likely to be the fracture from which the dome extruded one month later. Similarly, the coherence map for this date shows poor coherence within the fracture (**Fig 7.A**). Precision on the fracture is low (above 100 m), contrary to the rest of the plateau where there is a good vertical precision (between 2 and 5 m) (**Fig. 7. C**).

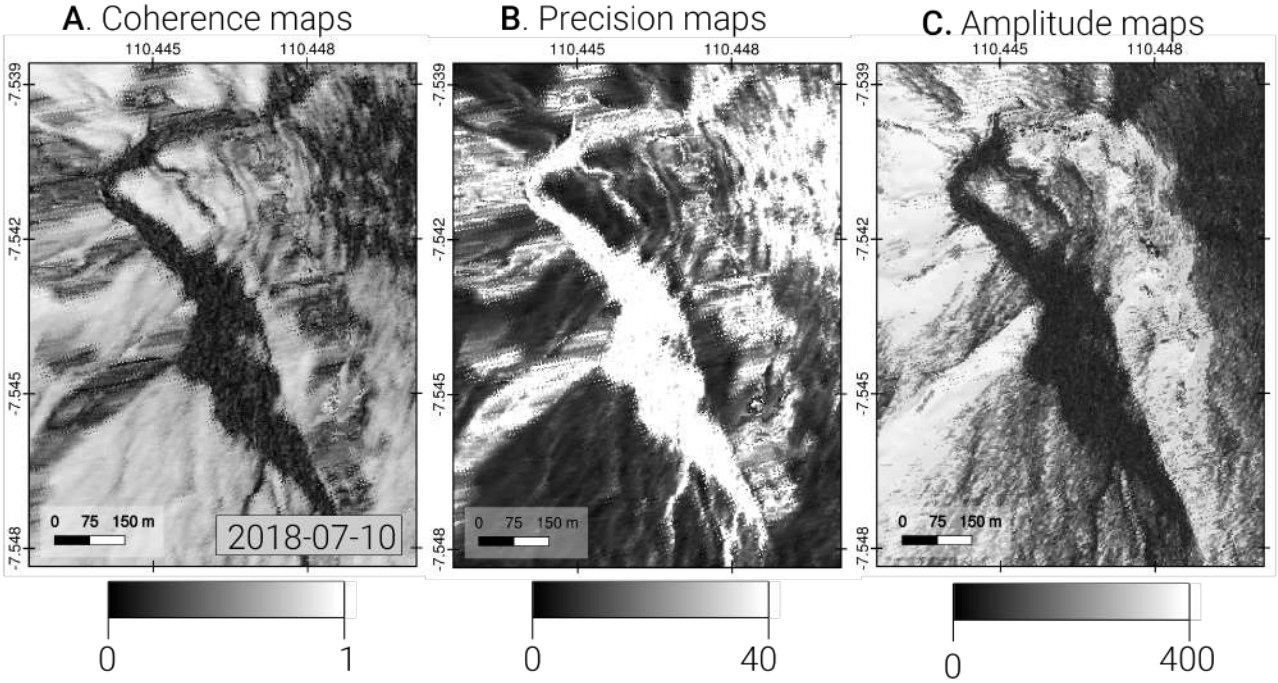

Figure 7. Coherence, precision and amplitude maps for the first image of the TanDEM-X dataset, acquired on 10 July 2018. The northwest-southeast oriented central fracture on the pre-existing plateau is clearly evidenced on the maps. Note that the ascending acquisition mode does not image the western flank of the valley below the plateau, nor the western wall of the crater.

4.2.2 Growth stage

Starting 23 August 2018, a new small shadow appears on the eastern side of the crater on both amplitude and coherence maps, and continues to grow until 09 March 2019, after which the size of the shadow remains constant until 08 July 2019 (**Fig 8**). According to the BPPTKG, the dome appeared on 11 August 2018, with the first aerial picture taken the day after. We interpret this shadow as the shadow of the dome due to its elevation: it is a qualitative way to visually assess the dome growth between August 2018 and March 2019. The false composite maps provide additional information to track the activity of the dome. First, they show that apart from the crater, the flanks of the volcano ground properties remain constant (yellow). Then, within the crater, the zone where the amplitude increases due to the rough properties and increasing slopes of the new extruded lava (cyan) enlarges between August 2018 and March 2019, with respect to the reference date of 10 July 2018. This method enables the tracking of dome growth both in area and height. More precisely, images from 23 August and 03 September 2018 show the shape of the rougher zone is almost radial, whereas it later extends asymmetrically to the northwest. On the other side of the fracture, a dark red zone also increases with time until March 2019, corresponding to the increasing shadow of the growing dome. From March 2019 to July 2019, this shadow remains constant.

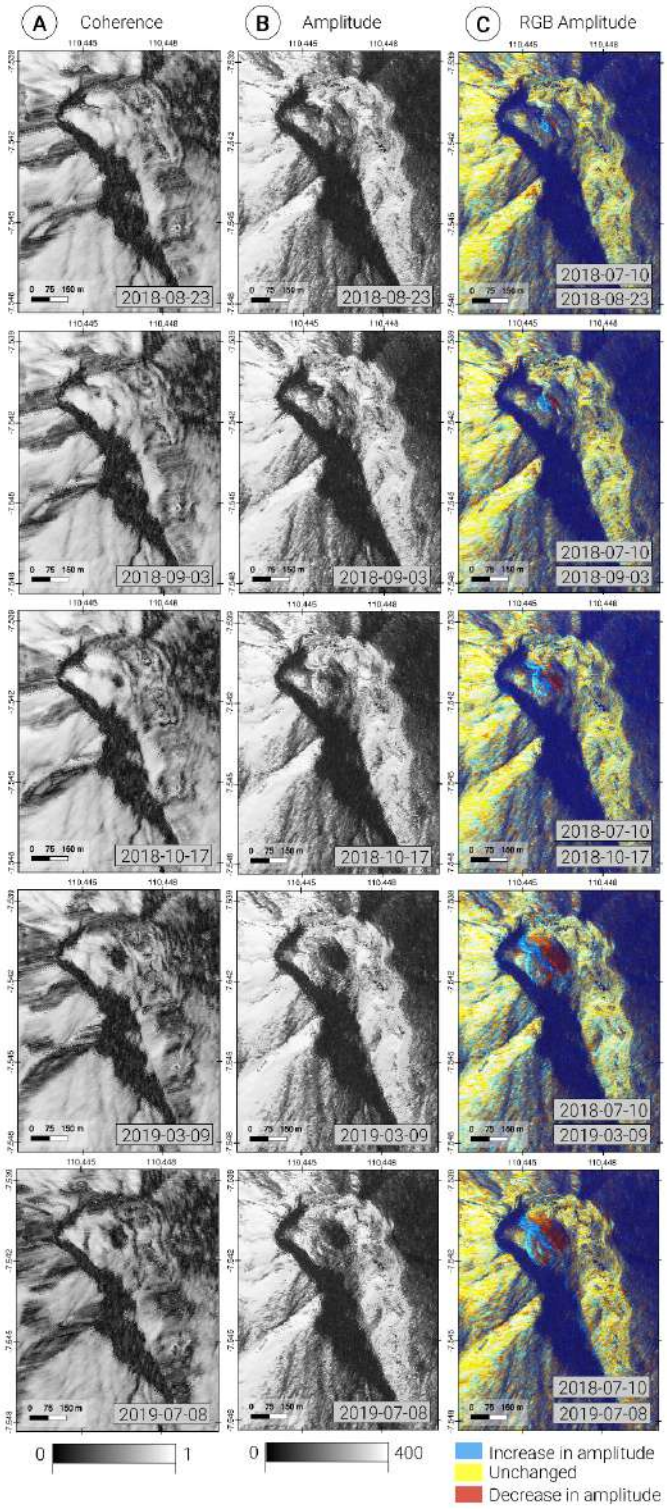

Figure 8. Coherence, amplitude and false color composite amplitude maps for 23 August 2018, 03 September 2018, 17 October 2018, 09 March 2019, and 08 July 2019. The growing shadow of the dome enables tracking dome growth of the dome between August 2018 and March 2019 on coherence and amplitude maps. The false color composite maps provide additional information on the slope changes between the first date prior to the dome (10 July 2018) and the given date. They reveal that at least until 03 September 2018 the dome has a radial shape and seems to extend to the northwest starting

17 October 2018 at the latest. The shape of the dome remains the same from 09 March 2019 to 08 July 2019, as the two last rows are identical.

The DEMs of 23 August, 03 September, and 17 October 2018 evidence the rapid growth of the dome from 8 meters to 25 meters high at the top, within only three months (**Fig 9 and corresponding profiles in Fig 10**).

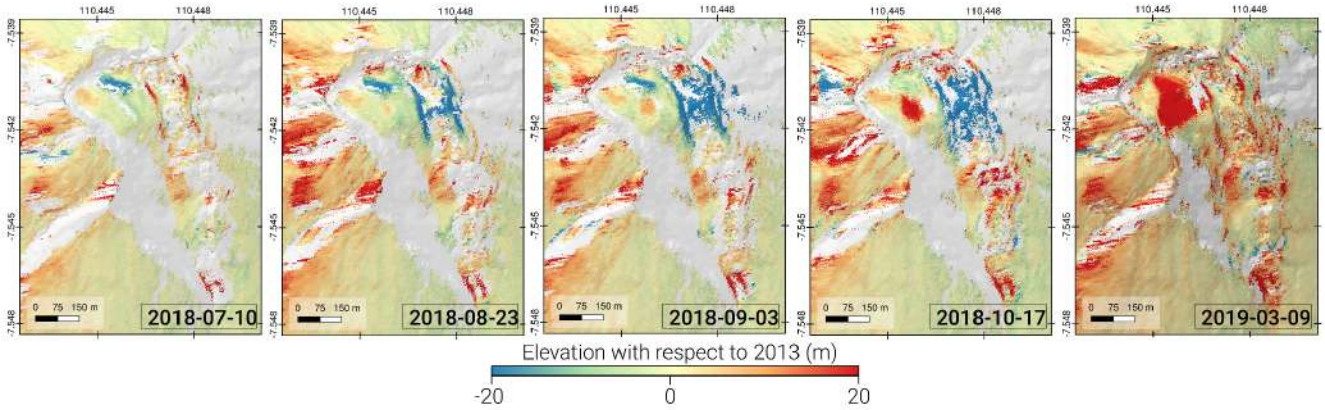

Figure 9. TanDEM-X derived DEMs for the growing stage, areas with a coherence below 0.6 being masked and DEMs are superimposed on the hillshade of 2013 DEM. The time series evidences the growth of the dome in the center of the crater up to 20 m high. Please note the important outliers on the flanks of the volcano (mainly on the east crater wall), due to potential residual unwrapping errors in areas characterized by a strong foreshortening.

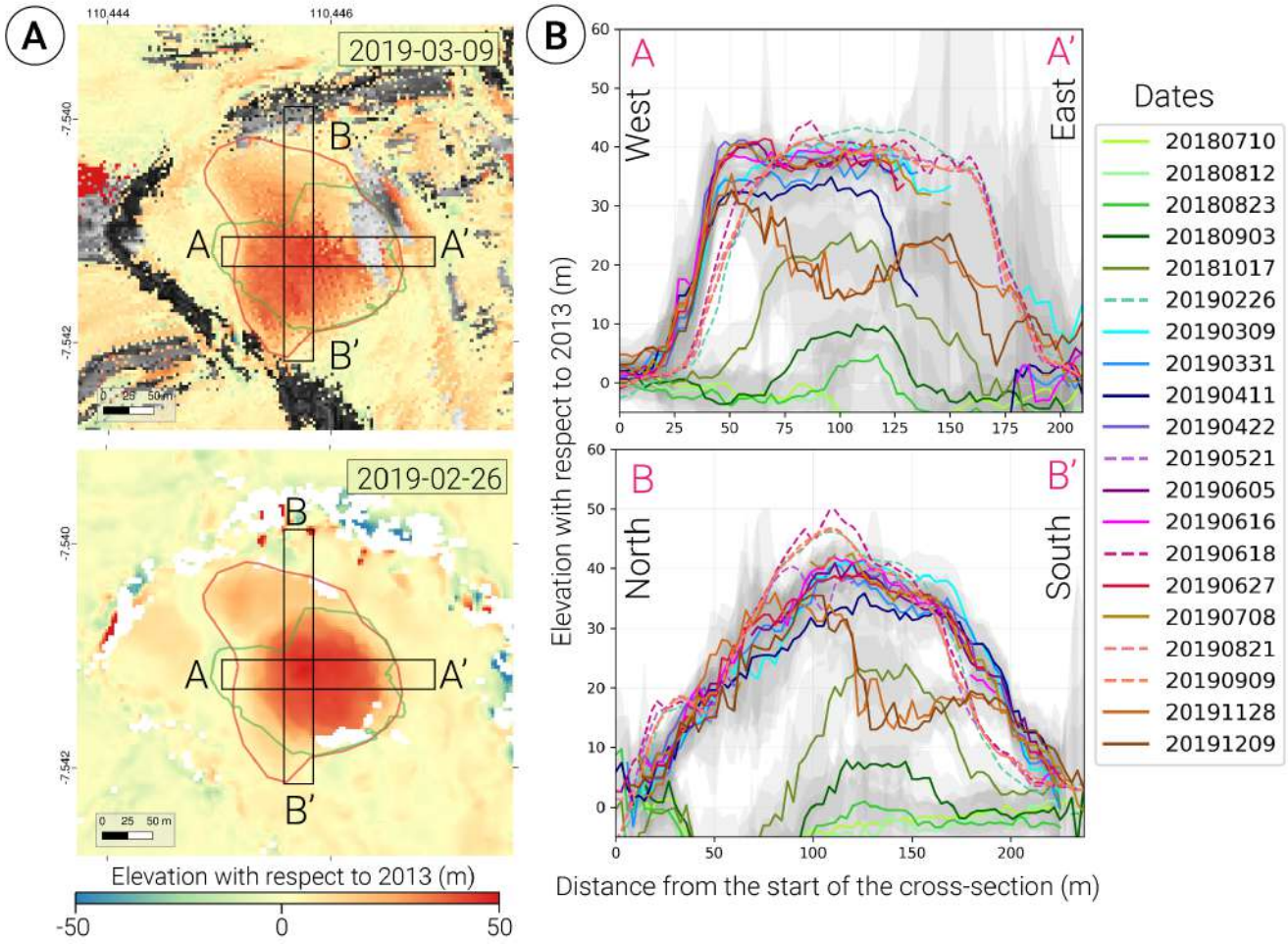

Figure 10. **Mean cross sections of the TanDEM-X and Pléiades derived DEMs and precision as uncertainties. Panel A**: location of the windows of the respective cross-sections in black boxes. The red outline corresponds to the outline derived from the DEMs of this study (Remote Sensing RS outline), the green outline corresponds to the outline of the surface monitored by drone flights (BPPTKG outline) . Top image is the TanDEM-X DEM of 09 March 2019, bottom image is the Pléiades DEM of 26 February 2019, both zoomed on the dome. **Panel B**: West-east cross section along A-A' in top box, and north-south cross section along B-B' in bottom box (boxes used to derive the profiles are ten pixels wide). Dotted lines correspond to Pléiades DEMs and continuous lines refer to TanDEM-X DEMs elevations. The filled gray zones behind correspond to the respective mean precision along the cross-sections. Please note that on the west-east cross-section, precision is very low on the eastern side of the dome due to the shadow resulting from the elevation of the dome in the line of sight of the satellite (LOS).

4.2.3. Steady stage

After March 2019, the growth phase is followed by a period of six months with no significant change in the morphology of the dome. We also performed a false composite map during the period where the size of the shadow of the dome remains constant: we take as the first date 09 March 2019 and as the second date 08 July 2019. The map evidences a cyan colored zone in the dome, meaning there was new

income of rougher material (lava) during this period even though the dome shadows suggest there are no more elevation changes.

Starting 09 March 2019 up to 08 July 2019, seven DEMs show the same elevation pattern without significant changes (see corresponding profiles in **Fig.10**). The dome top elevation rises to about 40 meters, with steep slopes.

4.2.4. Partial destruction stage

The two last dates of our TanDEM-X dataset are 28 November 2019 and 09 December 2019. Both show a partial decrease of the extent of the shadow on the eastern part of the dome, probably linked to the removal of some material of the dome (**Fig 11**).

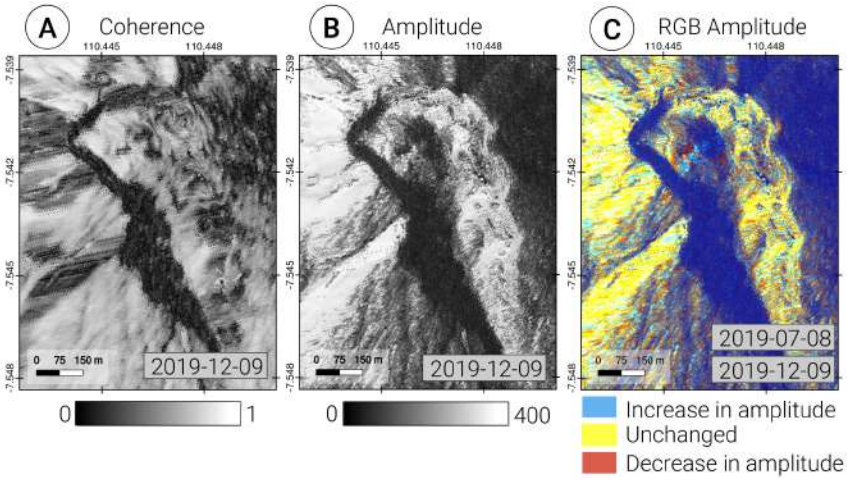

Figure 11. End of the dome growth evidenced by coherence, amplitude and RGB composite amplitude maps for 12 December 2019. **Panel A**: coherence map showing loss of coherence on the central part of the dome. **Panel B**: amplitude map showing similar information as coherence map. **Panel C**: false color composite map with the blue component corresponding to the difference between 08 July 2019 and 12 December 2019. It shows the decreasing amplitude corresponding to a potential loss of height, as well as an increase in amplitude to the south, that might correspond to some new rough material.

The partial destruction of the dome by explosion is also clearly visible in the DEMs. On 28 November and 09 December 2019, a central depression of more than 10 meters is evidenced on the west-east cross-section, and a depression of the same scale is identified to the south on the north-south cross-section (see corresponding profiles in **Fig 10**).

4.3. Comparison between TanDEM-X and Pléiades

Cross sections of the lava dome enable the tracking in space and time of the main topographic changes. We compute the mean west-east and north-south cross-section within a chosen window of ten pixels, in order to increase the signal to noise ratio (**Fig 10**). We take the vertical precision as an indicator of the uncertainties of our data.
The fifteen TanDEM-X derived DEMs provide quantitative information on the elevation changes of the dome. The maps provide information except in areas where unwrapping was not successful, mostly characterized by low coherence. As shown in section III.3, the precision of elevation derived from

TanDEM-X data depends on the height of ambiguity (precision decreases with increasing height of ambiguity). However, we consider that TanDEM-X data provide reliable information on the dome topography for a height of ambiguity as large as 100 m. For example, DEMs from 11 April and 22 April 2019 have respective heights of ambiguity of 105 and 44 m, and the dome morphology and heights are very close - the mean difference is only 0.46 m (see **Fig. 10**).
Vertical precision and pixel resolution in the ground range of TanDEM-X DEMs vary within the dome, as a consequence of radar acquisition geometry as detailed in section III.3. It should be noted that precision on the eastern flank of the dome is very low, due to the low coherence explained by the shadow of the dome on the plateau. Therefore the elevation in this area should not be considered as accurate for interpretation. Similarly, on the north-south cross-section, precision is low on the edges of the dome, on the wall of the crater to the north and the edge of the plateau to the south. TanDEM-X and Pléiades derived DEMs show very similar trends in the morphological evolution of the 2018-2019 dome on Merapi, which can be considered as a strong validation of both methods on a relatively small dome size. However, some differences evidenced by the cross-sections shouldn't be neglected. The west-east mean cross-sections global pattern shows that the edges of the west and east flanks are not at the exact same location (**Fig 11.B**). Pléiades derived DEMs provide a wider extent of the dome, especially to the east. This can be explained by the very low precision of the TanDEM-X derived DEMs on the eastern edges as it is shadowed. TanDEM-X DEMs probably lead to an underestimation of the dome extent on the east flank. On north-south cross-sections, TanDEM-X DEMs evidence a slightly wider and flatter dome than Pléiades DEMs.

4.4. Volume and effusion rate estimates

From dome surface manual mapping, mean volumes were computed in order to track the eruptive activity of the dome (**Fig 12**). Following the volumetric evolution of the dome is crucial for hazard assessment, as the hazard usually increases with growing and renewed quantity of unstable material. In this study, lava volumes correspond to lava effusion and accumulation building up the dome (refer to Kelfoun et al., 2021 thermal time series). TanDEM-X derived volumes track the rapid growth of the dome, a later stage with no topographic changes, followed by partial destruction of the central part of the dome. Pléiades derived volumes only track the volumes of the dome from the period with no major topographic change due to acquisition dates falling within this period only, but also provide a volume estimate of the accumulation area below the dome. This deposition zone also undergoes topographic changes, and tracking these changes is crucial for hazard assessment as well, as it might be unstable fresh material.
For the dome, volumes estimated from our outline are higher than volumes derived from the BPPTKG outline as we include the north-west increasing topography structure in the dome outline. We consider this latter definition of the dome outline relevant in our study, as we are interested in the quantity of incoming material to evaluate the activity of the dome. We focus on the volcanic behavior of the dome, not only for immediate monitoring purposes, but also for global dome understanding and modeling. Indonesian authorities, on the other hand, are more interested in assessing the maximum height of the dome for the monitoring and risk assessment, because the higher the dome, the more likely it will destabilize. Therefore, we mostly consider volumes derived from the RS outline for the dome as the best estimator of the volume, and we use the BPPTKG outline for comparison with the drone estimates.

Considering the RS outline on TanDEM-X DEMs, the dome reached a maximum volume of 0.26 Mm^3 by October 2018. During this early growth stage (August 2018-February 2019), the dome produced lava at a rate of 0.0336 ± 0.0067 $m^3.s^{-1}$ (2900 ± 580 m^3/day). Then volumes remained roughly constant

with a total mean volume for the dome of 0.64 ± 0.03 Mm^3 considering the period February-September 2019, using RS outline on both TanDEM-X and Pléiades. Pléiades and TanDEM-X DEMs separately provide a similar mean volume estimate during this period, of 0.64 ± 0.02 Mm^3 and 0.66 ± 0.01 Mm^3 respectively. The BPPTKG outline provides smaller estimates of lava dome volumes: a volume of 0.47 ± 0.03 Mm^3 considering both datasets, 0.46 ± 0.03 Mm^3 with TanDEM-X only, and 0.49 ± 0.02 Mm^3 with Pléiades only. This confirms that TanDEM-X and Pléiades DEMs are complementary and consistent when used together to estimate lava dome volumes.

Using the Pléiades dataset, we also estimated the accumulation zone volume. The accumulation zone by September 2019 reached a maximum volume of about 0.37 ± 0.29 Mm^3 and an accumulation rate of 0.0094 ± 0.001 $m^3.s^{-1}$ (810 ± 90 m^3/day) between February-September 2019.

To validate the TanDEM-X and Pléiades methods for estimating dome volumes, we compared our volumes derived from DEMs (using the BPPTKG outline) to independent daily volumes measured by BPPTKG drone flights. We show that volumes of the dome derived from DEMs are fully consistent with volumes computed from the drone. The mean volume estimated by the drone using photogrammetry is 0.46 ± 0.01 Mm^3 and for our DEMs is 0.47 ± 0.03 Mm^3. The effusion rate during the growth stage is similar for the drone and for TanDEM-X, respectively 0.0336 ± 0.0010 $m^3.s^{-1}$ (2900 ± 90 m^3/day) and 0.0249 ± 0.0053 $m^3.s^{-1}$ (2150 ± 460 m^3/day). We note that TanDEM-X provided slightly higher volume estimates than the drone at the early stage of dome growth, which might be an overestimate. For August 23, 2018, we measured with TanDEM-X DEM a volume of 0.04 Mm^3 whereas the drone measured a volume of 0.02 Mm^3. On the contrary, during the "steady" stage, TanDEM-X and Pléiades measured very similar volumes to the drone volumes. This confirms the reliability of both TanDEM-X and Pléiades for dome monitoring.

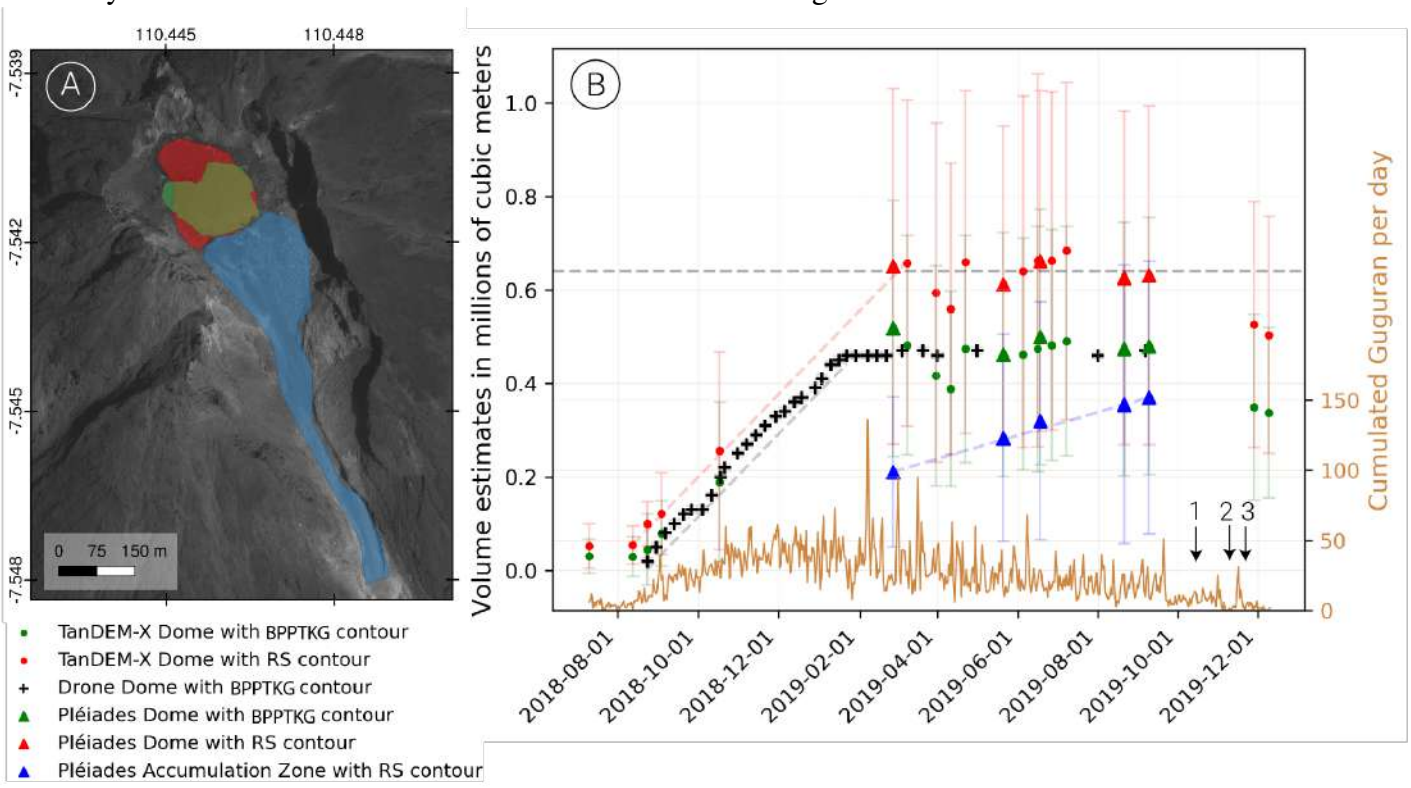

Figure 12. **Volume estimates from the dome and the accumulation zone**. **Panel A**: extent of the area where volumes were computed from TanDEM-X and Pléiades DEMs. **Panel B:** volume estimates and their uncertainties. The color of the marker refers to the type of outline that has been used to calculate the volume, and the marker type refers to the data type from which the volumes were derived.

The mean volume using both TanDEM-X and Pléiades between February-September 2019 is shown with the dashed gray line at 0.64 Mm^3. The effusion rates for TanDEM-X only and drone only on the dome are plotted as dashed lines, respectively red and black. The accumulation rate from Pléiades is plotted as a blue dashed line. The numbers 1, 2, 3 above arrows in the end of 2019 indicate dates when dome explosions were recorded : on 14 October 2019, 9 November 2019 and 17 November 2019, according to Kelfoun et al., 2021. Additional seismic data from WebObs is also presented to highlight that even though the volume of the dome remained constant between March-July 2019, small rock falls (referred to as Guguran, brown line) contributed in partially destroying the dome and supplying the accumulation zone with new material.

5. Discussion

5.1. Interpretation of chronology of events

Relying on the description of changes to the lava dome described by Kelfoun et al., 2021 using two cameras on the edges of the crater, we interpret the results observed on the DEMs derived from remote-sensing. First, the location and dimensions of the dome are consistent with their description. The timing is also consistent with ground-based observations: Kelfoun et al., 2021 describe a first radial growth until October 2018, followed by asymmetric growth oriented towards the northwest.

After this dome expansion, they observe the dome starts to destabilize first on the northwest flank, and then mainly on the southeast flank, with material falling into the Gendol gorge. They suggest destabilization is partly controlled by the accumulation of talus from the dome that reaches a certain slope threshold related to a change in rheology of the rock, triggering partial gravitational collapse. This observation is consistent with seismic records of increasing small rockfalls (Gugurans) recorded on Merapi (available on WEBOBS online) at this time (**Fig 12.B**). Gugurans increase as the dome grows with steeper slopes, resulting in gravitational instabilities on its edges (Ratdomopurbo and Poupinet, 2000). At the same time, multiphase events (also available on Webobs) are also numerous during the growth stage, up to about twenty events per day. These can be interpreted as lava effusion contributing to dome growth, whereas Gugurans are related to volume loss even if the dome is still growing. Another study by Darmawan et al., 2020, using high resolution optical cameras in April 2019, also confirms decameters to meters-scale destabilization of the central and south parts of the dome, leading to scars on its edges.

This observation of destabilization on the talus part of the dome is consistent with observations on other domes : it seems the dome first grows vertically and later expands laterally on the talus area, and potentially collapses due to slope and modification of the rheological behavior of the rock (Zorn et al., 2020 ; Harnett et al., 2018 & 2021). Moreover, Zorn et al., 2019 suggest the directional expansion of the dome could be a hint on its instability, even though the reasons why a preferential direction is taken are not fully understood. In our case, we observe the lateral expansion of the dome first to the northwest after a radial phase, followed by a change of direction toward the southeast, constrained by topography (the crater wall to the northwest). This is supported by Walter et al., 2013b that suggest that the crater shape plays a role in the orientation of the dome flow. Zorn et al., 2019 also suggest that load removal from the dome, as in our study with falling blocks in the Gendol valley, can maintain lava extrusion due to stress changes in the local, shallow conduit, which we also observe as material loss is balanced by lava accumulation.

While some parts of the talus detach from the dome, Kelfoun et al., 2021 still observe lava emission from the dome. This suggests that the constant topography we observe on our DEMs, from February to

September 2019, is the result of a balance between lava gain in the dome and loss from rockfalls, driven in the Gendol gorge. We could therefore consider the estimated accumulation rate in the Gendol valley, with Pléiades, as a proxy for the ongoing extrusion rate at the dome during this "steady" period. The production of lava during this period of no elevation changes is evidenced thanks to the TanDEM-X amplitude false color composite map between March and July 2019: rougher material is detected, that is probably due to new lava extruding between these two dates.

All these independent observations confirm the partial destruction of the dome starting early 2019 on the southeast edges of the crater, balanced by the continuous effusion state of the dome, thus explaining the absence of major topographic changes of the dome until September 2019. Starting September 2019, Kelfoun et al., 2021 identify several explosions occurring in the crater, leading to partial destruction of the southeast edges of the dome, which is also consistent with our cross-sections. The authors suggest that due to the slopes of the dome exceeding 35°, the dome couldn't grow within its external slopes, resulting in continuous destabilization of blocks of talus for almost one year, without any real risk as they were rapidly depositing downward in the Gendol gorge. This behavior could have prevented the dome from reaching the critical state and generating PDCs that would have threatened the population. The authors suggest the morphology of the dome at the summit would therefore influence the evolution of the dome into either gravitational collapse or more hazardous explosive events. Our study provides additional support for such a hypothesis, as ground-based measurements only partially observe the dome. We provide spatially continuous maps of the whole dome, and have the ability to estimate the deposits in the Gendol gorge, which is currently not possible using only ground-based cameras. Similar observations of dome growth and stability before partial destruction have been done, for example Diefenbach et al., 2013 on Redoubt volcano. The authors suggest the dome could be stable because of the open-shaped crater that allows lateral extension before reaching a threshold where material flows downslope.

5.2 Effusion rates

Dome growth rates and duration have long been recognised as key information for inferring the probability of an explosive eruption and its intensity (Newhall et al., 1983). In particular, the likelihood of an eruption following dome growth being highly explosive (VEI>4) increases with the rate of extrusion (Ogburn et al., 2015). For the 2018 dome growth episodes at Merapi volcano, which lasted about two hundred days, between August 2018 - February 2019, the extrusion rate was estimated, in this study, to be around 0.0336 $m^3.s^{-1}$ (and 0.0336 $m^3.s^{-1}$ also with drone estimates), which is at the lower bound of time-average discharge rates commonly observed for volcanoes of andesitic composition, ranging from to 0.035 $m^3.s^{-1}$ to several tens of $m^3.s^{-1}$ over short durations (see Supplementary material of Arnold et al., 2017). The extrusion rate observed during the 2018 dome growth episode is close to the long term trend recorded at Merapi volcano, where the average effusion rate over hundred years is 0.038 $m^3.s^{-1}$ (3280 $m^3.day^{-1}$) according to Siswowidjoyo et al., 1995. However, this value is small for a dome building episode (Pallister et al, 2013 ; Moussallam et al., 2021) and a volume of 0.64 Mm^3 is on the lower end of domes size (Moussallam et al., 2021 ; refer also to **Table 2**). The likelihood of an eruption immediately following this dome growth episode thus remained quite small as evaluated by the BPPTKG and the main concern was related to gravitational collapses when the dome reached the edge of the plateau. For comparison the effusion rate recorded before the 2006 eruption was larger by two orders of magnitude with peak rates around 4 $m^3.s^{-1}$

(Ratdomopurbo et al., 2013). The highest dome growth rates recorded at Merapi volcano reached 35 $m^3.s^{-1}$ and were observed just before the VEI 4 eruption, which occurred in early November 2010 (Pallister et al., 2013).

If we compare our study with other dome volume and effusion rate estimates (**Table 2**), the volume of 0.64 Mm^3 is of the same amplitude as other low volume domes for equivalent sizes estimated from optical imagery. It is similar, for example, to the size of the dome emplaced at Nevados de Chillan, Chile (Moussallam et al., 2021) or at Colima volcano, Mexico either in 2011 (Walter et al., 2013) or in 2013-2015 (Thiele et al., 2017). However, as mentioned previously, the Merapi 2018-2019 dome stands at the lower end of domes : if we look at Redoubt (Diefenbach et al., 2012), the dome has a width of 500 m for an average thickness of 200 m and a volume of 72 Mm^3 with a high effusion rate of at least 2.2 m^3/s, or the Soufriere Hills Montserrat (Wadge et al., 2011) with 1 km long dome lobes for a volume of 40-50 Mm^3.

References	Volcano/ Year	Method	Datatype	Dome width + height (m)	Volume (Mm^3)	Extrusion rate (m^3/s)	Vertical Precision (m)	Pixel size (m)
Our study 2022	Merapi 2018-2019	SAR amplitude + phase Optical SP	15 TanDEM-X 5 Pléiades Drone optical images	200 40	0.64	0.034	5	3
Wadge et al., 2011	Soufriere Hills 2008-2010	SAR amplitude	6 TerraSARX	~1000	~40	not indicated	m scale	2
Pallister et al., 2013	Merapi 2010	SAR amplitude	7 RADARSAT + 6 TerraSARX GeoEye 1 WorldView-2	~400*400 ~200	~14.50	25-35	not indicated	0.5 to 3
Kubanek et al., 2015	Merapi 2010	SAR phase	3 TanDEM-X	~400*400 ~200	~19	not indicated	2 to 4	3
Arnold et al., 2016	Soufrière Hills 1995-2010	SAR phase	ALOS + TanDEM-X	~900*900 ~290	108	not indicated	<10	10
Arnold et al., 2017	El Reventador 2011-2016	SAR phase + amplitude	32 RADARSAT-2+9 TanDEM-X	~200*200 20 to 30	0.99	0.069	meter scale	2.5 (amplitude) 6 (TanDEM-X DEMs)
Wang et al., 2015	Mt Cleveland 2011-2012	SAR amplitude	10 TerraSARX	40*40 70	not indicated	detectable : ~0.04 , maximum: 0.6	non indicated	1.5
Angarita et al., 2021	Shishaldin 2019-2020	SAR amplitude	Dozens of TerraSARX	200*200 20	0.1-0.15	not indicated	5	1
Andaru et al., 2019	Agung 2017	Optical SP InSAR	UAVs with optical cameras Sentinel 1-A	not indicated	not computed	not computed	not indicated	0.66-1.79 (optical)
Walter et al., 2019	Colima 2013	SAR amplitude Optical pixel offset	9 TerraSARX Ground-based optical camera	160 along NE-SW 20	0.032	not computed	not indicated	2 (radar) 0.1 (optical)
Zorn et al., 2019	Colima 2013-2016	SAR amplitude Optical SP	166 TerraSARX 13 aerial models	~100 *100 ~30	not done	not computed	not indicated	1 (amplitude) 0.1 (optical)
Zorn et al., 2020	Santiaguito 2019	Optical SP + Pixel offset Thermal Pléiades as reference	UAVs with optical and thermal cameras	200*200 ~50	0.0005	0.04-0.06	<0.3	0.7 (optical) 0.45 (thermal)
Walter et al., 2022	Shiveluch 2020	SAR amplitude pixel offset Optical SP	6 TerraSAR-X Ground-based + aerial optical camera 3 Pléiades	~300*300 ~220	not indicated	0.3–0.7	2.35 (ground-based) 0.2 (Pléiades)	6.8 (ground-based) 1 (TerraSARX) 2 (Pléiades)
Ordonez et al., 2022	Nevado del Ruiz 2015–2021	SAR amplitude Optical SP	37 TanDEM-X + 30 TerraSARX 2 aerial models 3 Planet Labs	~130*130 ~60	1.7 ± 0.2	~0.19 in 2015 0.02 in 2018	not indicated	2.5 (radar) 10 (optical)
Herd et al., 2005	Colima 2013	Optical cross sections	Ground-based optical camera	300*300 400	~164	not computed	not indicated	not indicated
Ryan et al., 2010	Soufrière Hills 2005-2008	Optical SP	Ground-based optical camera (+ radar + LIDAR)	not indicated	306	5.6	not indicated	not indicated
Diefenbach et al., 2011	St Helens 2004-2007	Optical SP	12 aerial models	1000*600 371	94±0.9	0.3	1.3	2
Diefenbach et al., 2013	Redoubt 2009	Optical SP	10 aerial models	500*1000 200	72	9.5	not indicated	10
Darmawan et al., 2018	Merapi 2012-2015	Optical SP	2 aerial models	150*200 30-70	~0.2	not indicated	0.2-0.6	0.5
Moussallam et al., 2021	Nevados de Chillan 2017-2019	Optical SP	7 Pléiades 12 aerial models	35*22 (2017), 119*79 (2018) ~30	0.4	0.02 in 2018 0.001 in 2019	0.48 (Aerial) 1 (Pléiades)	0.1 to 1 (Aerial) not indicated (Pléiades)
Walter et al., 2013	Colima 2011	Thermal pixel offset	Ground-based thermal cameras	184*184 height not indicated	not computed	not computed	0.5	1
Carr et al., 2016	Merapi 2006	Thermal InfraRed radiance	75 MODIS + ASTER	150*150 height not indicated	8.4	maximum 7.5 average 0.2	not indicated	<100
Thiele et al., 2017	Colima 2013-2015	Thermal + optical cameras SP	22 aerial thermal models 19 optical models	140*140 ~60	1.05 (thermal), 1.16 (optical)	not indicated	not indicated	not indicated

Table 2. Dome dimensions, volume and extrusion rate estimates for other volcanoes, using various remote sensing methods. Note some papers did not estimate volume or extrusion rate estimates due to the method itself hindering a 3D view of the dome, as it is the case for radar amplitude, ground-based optical or thermal cameras studies. SP stands for StereoPhotogrammetry, meaning DEMs were produced ; UAV stands for Unmanned Aerial Vehicle.

Yellow colors indicate methods using mostly SAR, green colors indicate methods using both aerial or ground-based optical cameras and SAR, orange colors indicate methods using mostly aerial or ground-based optical cameras, and blue colors indicate methods using thermal images. Our study is the only

one to use both bistatic SAR data and optical satellite data acquired in stereo mode to track a dome growth episode.

5.3. Comparison with other lava dome studies methods

While other studies of crater-hosted lava domes (**Table 2**) have used a wide range of methods (radar, optical, thermal), none use high-resolution satellite radar and satellite optical data together to retrieve DEMs. A few papers attempt to use the maximum available remote data to track topographic changes during dome events (e.g. Ordonez et al., 2022 ; Walter et al., 2022), but without using SAR phase.

Studies using SAR mostly rely on amplitude analysis to deduce height changes, but rarely DEMs. For example, Wang et al., 2015 retrieve heights thanks to the amplitude through modeling of the dome, Walter et al., 2019 use RGB composite maps of amplitude to qualitatively assess changes, Angarita et al., 2022 retrieve topography thanks to gradient from the amplitude, Arnold et al., 2017 and Wadge et al., 2011 use the shadow from the amplitude. These studies relying on SAR are sometimes compared to airborne optical images (e.g. Walter et al., 2019 ; Zorn et al., 2019). We only record two studies using SAR phase from TanDEM-X to build DEMs. Kubanek et al., 2015 demonstrated that TanDEM-X was a powerful tool for monitoring changes at the top of Merapi using DEMs. Following this milestone, Arnold et al., 2017, on El Reventador, use both TanDEM-X phase and RADARSAT repeated-pass amplitude shadowing to assess topographic changes, volumes and effusion rates. However, neither of the latter two studies uses optical satellite images as additional data. In addition, the studies using satellite radar rely mainly on amplitude analysis, with repeat-pass interferometry being more common and easier to access than bistatic datasets.
In our study, we take advantage of both the phase and the amplitude of the radar to infer as much information as possible about the dome. We also provide a well-resolved time evolution: Kubanek et al., 2015 used three DEMs to track changes in one month, while we use fifteen DEMs from TanDEM-X to track changes over more than one year. Furthermore, we are able to provide a quantitative estimate of our uncertainties, which is not systematically available in the literature (see **Table 2**).

Looking at studies involving optical imagery, the vast majority of them rely on either ground-based or airborne cameras, Pléiades being only additional data to validate results. Ground-based (Walter et al., 2019 ; Herd et al., 2005 ; Ryan et al., 2010) and aerial flights (Zorn et al., 2020 ; Moussallam et al., 2021) have the advantage of providing better resolute views of a dome, but require specific campaigns that are costly in time and can only cover smaller areas. The limitations of optical imagery often lead to use this method jointly with other tools : thermal imagery (Thiele et al., 2017) or SAR amplitudes (Ordonez et al., 2022). One reason explaining the limited number of studies using Pléiades is data availability. To our knowledge, the only studies using Pléiades are the ones from Moussallam et al., 2021 and Walter et al., 2022. Ordonez et al., 2022 use Planet Labs which are also satellite optical imagery.

5.4. Advantage/Disadvantages of TanDEM-X data compared to Pléiades data

Both Pléiades and TanDEM-X space imagery provide high spatial resolution products to generate high resolution DEMs of the dome area. In this study we have shown that both methods provide consistent DEMs and can be used together to construct DEM time series with better temporal resolution. We have also shown that these data allow the monitoring of small domes with a volume of less than 1 Mm^3 characterized by a low effusion rate. This means that, considering similar uncertainties, the monitoring

of larger domes, with a higher effusion rate, should be even more robust. The main remaining limitation for the use of these high resolution data is due to the fact that they are neither routinely acquired nor provided as open data, but rather are only available on demand through dedicated proposals with limited access.
We discuss in the following section the specific interest to use TanDEM-X and Pléiades in the tracking of a lava dome: both are crucial tools that could be more widely developed in observatories, when the access to the volcano is difficult (e.g remote, steep sloped or active volcano) for routine monitoring, or when an effusive eruption is ongoing (e.g this study). Explosive eruptions might be more difficult to monitor with optical methods, mainly due to the presence of ash plumes.

The main advantage of TanDEM-X data is the return time of only eleven days, thus opening possibilities to build DEMs time series with high temporal resolution. They have proven to be suited and efficient for tracking other volcanic activity such as lava flows (Kubanek et al., 2017), PDCs (Albino et al., 2020) and crater morphology (Kubanek et al., 2015). However, they lack full spatial coverage due to the grazing incidence of satellites: the slopes around the dome and in half of the Gendol gorge are very noisy and can't be unwrapped, resulting in a lack of data. Results also have to be interpreted with respect to coherence maps that reflect the quality of the data. Another consequence of the geometry of acquisition is that a previous selection of tracks showing best visibility needs to be done in order to continuously map the area of interest, using ground resolution maps for instance (Albino et al., 2020). Ground resolution maps depend on the local incidence of the radar wave with respect to the slopes of the volcano, and indicate areas where shadowing or layover will occur. A high resolution reference DEM also needs to be available for optimal interferogram generation.

Our study proves Pléiades are crucial data for effective monitoring of an active summit area. When Pléiades stereo-pairs or triplets can be used, they have the advantage to be easily and rapidly processed in a fully automated processing chain, although the final step of DEM offset correction still needs to be done manually. Even though Pléiades has the advantage of providing a wide view of the dome and the associated deposits, it is highly dependent on daylight and good weather conditions. Therefore, acquisitions can not be equally spaced in time, resulting in a sparser temporal resolution. Moreover, the accuracy we obtain with Pléiades is worse than aerial optical images, but the spatial extent of the image offers the capability to track larger areas and to eventually bypass field campaigns if weather conditions are bad.

Radar and optical DEMs should also be compared to GPS measurements to improve the monitoring, although installing stations on the dome itself would be too hazardous. Our study uses a drone carrying optical cameras to validate our results : we prove satellite and aerial data are consistent with one another. The ultimate aim of dome monitoring would be to understand what controls dome destruction and if there are signs to forecast its onset.

5.5. An alternative method to rapidly estimate heights from radar images

We also tried to estimate the height of the edge of the dome using the shadow of the amplitude and coherence maps. Shadow was more contrasted on coherence maps than on amplitude maps. Assuming the shadow on coherence maps is only due to the geometry of the dome thanks to the bistatic mode of acquisitions, we measured the length of the shadow on a west-east line and follow the strategy of Wadge et al., 2011 for a flat bottomed valley with flat deposits, considering the plateau on which the dome builds up is flat (**Fig 13.A**). The relationship is $h_1=g_1*\cot(\Theta)$, with Θ the incidence angle, h1 the

edge of the dome of height, and g_1 the width of the shadow of the dome. We compare these heights with the ones from the DEMs (See TanDEM-X DEMs section) and the ones from shadows on amplitude maps. The method relies on the use of the propagation path of the wave along the crater wall and the dome. We show that for height estimates based on coherence, there is a difference of 10-20 m between mean height estimates from the DEMs on the eastern edge of the dome, but that the evolution of the height over time is similar (**Fig 13.B**). Furthermore, when considering the maximum height of the dome only, estimates from coherence shadow are very similar to estimates from the DEM. On the contrary, height estimates from amplitude have a bigger offset to the estimates from DEMs, but the variations are similar. We consider this method relying on the shadow can be a good first approximation to follow the relative evolution in time of the height. But the method from shadow is not sufficient to get the absolute height as the uncertainties are too high, mainly because of the manual estimation of the limit between shadowed and non shadowed area. Moreover, we also assume the top of the dome and the plateau are flat. However, it can be a useful tool in case of monitoring and/or when bistatic acquisitions are not available, as a first order proxy for evolution of the height of the dome.
Alternatively, a recent study by Angarita et al., 2022 proposes a new method to derive DEMs from radar amplitude images using the relationship between the backscatter properties and the local topographic slope. This tool requires an inversion to retrieve the topography but could be promising to reconstruct DEMs without the need of bistatic acquisitions.

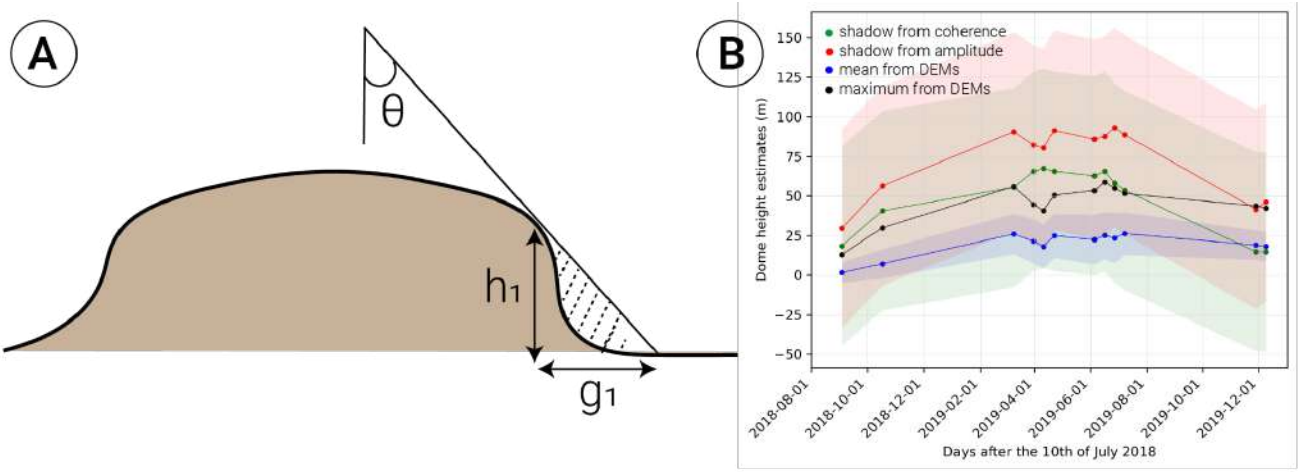

Figure 13. Height of the eastern border of the dome using TanDEM-X elevations from the DEMs and elevations estimated from the coherence maps shadow. Panel A: Scheme of the geometrical parameters to deduce the height of the dome from its shadow (adapted from Wadge et al., 2011). **Panel B:** Height estimates and their respective uncertainties. Green dots refer to height estimates from shadows on coherence maps, red dots to estimates from shadows on amplitude maps, blue dots refer to the mean height from DEMs within the drone outline, and black dots refer to maximum dome height from DEMs for each date.

6. Conclusion

This study of the evolution of the lava dome on the Merapi between 2018 and 2019 provides information on the behavior of a lava dome before it is destroyed, as well as methodological improvements for the monitoring of the activity of the dome of a steep sloped stratovolcano. Dome building stratovolcanoes such as the Merapi are highly difficult to monitor with ground based instruments and are among the most dangerous volcanoes. As a consequence, remote sensing tools are crucial to assess volcanic risk safely and efficiently as their spatial and temporal resolution keep

improving. In this study, we take advantage of two high resolution remote sensing imaging satellite systems to estimate heights and volumes of the dome. We use TanDEM-X and Pléiades radar and optical images to build a partially complete time series of DEMs, with a DEM almost every month. The accuracy of each method for estimating heights and volumes is assessed by statistical error estimates and validated by comparison with additional, independent volume estimates from thermal imaging cameras and drone measurements.

Using TanDEM-X and Pléiades derived DEMs, we show that the dome first appears on a pre-existing fracture on a pre-existing dome within the crater of the volcano, then grows radially and asymmetrically, reaches a stage where no more topographic change is recorded, and is finally partially destroyed in its center by explosions. However, during the period when the dome maintains a constant topography, new material continues to reach the surface, indicating that the dome is still active. Pléiades DEMs allow mapping an accumulation zone below the dome: this suggests there is a balance between the addition and destabilization of material, explaining its constant topography. This pattern of dynamics can be of great use to better understand what triggers dome growth and collapse. Our study provides new insights and observations on a possible mechanism ruling dome stability : on the one hand the lava dome seems to reach a critical threshold regarding height, dimensions and slope, and on the other hand, the instability leading to rock falls could be a mechanism explaining renewed lava supply.

Our study also proposes a new monitoring strategy for small domes hosted within craters. This strategy is complementary to all other monitoring methods of lava domes. The fifteen TanDEM-X DEMs provide a good temporal resolution of the dome evolution, whereas the five Pléiades DEMs increase the spatial extension of the mapping as they also enable the tracking of deposits south of the dome, in the Gendol gorge. Here, we prove that both Pléiades and TanDEM-X DEMs are effective and complementary to map lava domes of small dimension on a steep sloped volcano, therefore extending the capabilities of these satellites in volcano monitoring. They are also able to be used in conjunction with drone surveys. We also show that amplitude and coherence maps resulting from TanDEM-X data provide complementary information to the interpretation of DEMs, by evidencing renewed magma supply of the dome even though no elevation change is detected. We suggest TanDEM-X and Pléiades derived DEMs are relevant tools to assess lava dome evolution on stratovolcanoes, and propose a wider use of these datasets in observatories, as well as constraints for numerical models.

CRediT authorship contribution statement

Shan Grémion: Conceptualization, Formal analysis, Software, Investigation, Writing, Visualization, Validation ; **Virginie Pinel**: Funding acquisition, Data Curation, Project administration, Resources, Supervision, Methodology, Conceptualization, Formal analysis, Software, Validation, Writing; **Tara Shreve**: Methodology, Conceptualization, Formal analysis, Software, Writing; **François Beauducel:** Project administration, Resources, Supervision, Writing **, Raditya Putra:** Methodology, Data Curation, Validation**, Akhmad Solikhin:** Methodology, Validation **, Agus Budi Santoso, and Hanik Humaida** : Validation

Acknowledgments

Pléiades data were made available by Airbus, DS through the Dinamis project 2018-155-Sci supported by CNES (©CNES_2013, distribution AIRBUS DS, France, all rights reserved and ©CNES_2019,

distribution AIRBUS DS, France, all rights reserved) and TanDEM-X data were provided by DLR through proposal XTI_GEOL7375. Many thanks to Pascal Lacroix for his help on the methodology for processing Pléiades images and to Fabien Albino for his precious advice and help on resolution and precision maps. The study was supported by the CNES projects AssimSAR and MagmaTrack, the Instrumented Site VELI (IRD), the Laboratoire Mixte International SIR (IRD).

Data Availability Statement

DEMs are available via the Zenodo repository (https://doi.org/10.5281/zenodo.7366725). It contains the DEMs under geotiff format along with a small description of the methodology to produce them, more detailed in this paper.

References

Abdurachman, E. K., Bourdier, J.-L., & Voight, B. (2000). Nuées ardentes of 22 November 1994 at Merapi volcano, Java, Indonesia. Journal of Volcanology and Geothermal Research, 100(1-4), 345-361. https://doi.org/10.1016/S0377-0273(00)00144-X

Albino, F., Biggs, J., Escobar-Wolf, R., Naismith, A., Watson, M., Phillips, J. C., & Chigna Marroquin, G. A. (2020). Using TanDEM-X to measure pyroclastic flow source location, thickness and volume : Application to the 3rd June 2018 eruption of Fuego volcano, Guatemala. Journal of Volcanology and Geothermal Research, 406, 107063. https://doi.org/10.1016/j.jvolgeores.2020.107063

Albino, F., Biggs, J., Yu, C., & Li, Z. (2020). Automated Methods for Detecting Volcanic Deformation Using Sentinel-1 InSAR Time Series Illustrated by the 2017–2018 Unrest at Agung, Indonesia. Journal of Geophysical Research: Solid Earth, 125(2). https://doi.org/10.1029/2019JB017908

Anantrasirichai, N., Biggs, J., Albino, F., & Bull, D. (2019). A deep learning approach to detecting volcano deformation from satellite imagery using synthetic datasets. Remote Sensing of Environment, 230, 111179. https://doi.org/10.1016/j.rse.2019.04.032

Angarita, M., Grapenthin, R., Plank, S., Meyer, F., & Dietterich, H. (2022). Quantifying large-scale surface change using SAR amplitude images: Crater morphology changes during the 2019-2020 Shishaldin volcano eruption. Journal of Geophysical Research: Solid Earth, e2022JB024344.

Arnold, D. W. D., Biggs, J., Anderson, K., Vallejo Vargas, S., Wadge, G., Ebmeier, S. K., Naranjo, M. F., & Mothes, P. (2017). Decaying Lava Extrusion Rate at El Reventador Volcano, Ecuador, Measured Using High-Resolution Satellite Radar : decaying lava extrusion rate at El Reventador. Journal of Geophysical Research: Solid Earth, 122(12), 9966-9988. https://doi.org/10.1002/2017JB014580

Arnold, D. W. D., Biggs, J., Wadge, G., Ebmeier, S. K., Odbert, H. M., & Poland, M. P. (2016). Dome growth, collapse, and valley fill at Soufrière Hills Volcano, Montserrat, from 1995 to 2013 : Contributions from satellite radar measurements of topographic change. Geosphere, 12(4), 1300-1315. https://doi.org/10.1130/GES01291.1

Bagnardi, M., González, P. J., & Hooper, A. (2016). High-resolution digital elevation model from tri-stereo Pleiades-1 satellite imagery for lava flow volume estimates at Fogo Volcano : Tri-stereo Pleiades DEM of Fogo volcano. Geophysical Research Letters, 43(12), 6267-6275. https://doi.org/10.1002/2016GL069457

Bato, M. G., Froger, J. L., Harris, A. J. L., & Villeneuve, N. (2016). Monitoring an effusive eruption at Piton de la Fournaise using radar and thermal infrared remote sensing data : Insights into the October 2010 eruption and its lava flows. Geological Society, London, Special Publications, 426(1), 533-552. https://doi.org/10.1144/SP426.30

Beauducel, F., & Cornet, F. H. (1999). Collection and three-dimensional modeling of GPS and tilt data at Merapi volcano, Java. Journal of Geophysical Research: Solid Earth, 104(B1), 725-736. https://doi.org/10.1029/1998JB900031

Beauducel, F., Lafon, D., Béguin, X., Saurel, J.-M., Bosson, A., Mallarino, D., Boissier, P., Brunet, C., Lemarchand, A., Anténor-Habazac, C., Nercessian, A., & Fahmi, A. A. (2020). WebObs : The Volcano Observatories Missing Link Between Research and Real-Time Monitoring. Frontiers in Earth Science, 8, 48. https://doi.org/10.3389/feart.2020.00048

Berthier, E., Arnaud, Y., Kumar, R., Ahmad, S., Wagnon, P., & Chevallier, P. (2007). Remote sensing estimates of glacier mass balances in the Himachal Pradesh (Western Himalaya, India). Remote Sensing of Environment, 108(3), 327-338. https://doi.org/10.1016/j.rse.2006.11.017

Calder. (2002). Mechanisms of lava dome instability and generation of rockfalls and pyroclastic flows at Soufriere Hills Volcano, Montserrat.

Camus, G., Gourgaud, A., Mossand-Berthommier, P.-C., & Vincent, P.-M. (2000). Merapi (Central Java, Indonesia) : An outline of the structural and magmatological evolution, with a special emphasis to the major pyroclastic events. Journal of Volcanology and Geothermal Research, 100(1-4), 139-163. https://doi.org/10.1016/S0377-0273(00)00135-9

Capra, L., Macías, J. L., Cortés, A., Dávila, N., Saucedo, R., Osorio-Ocampo, S., Arce, J. L., Gavilanes-Ruiz, J. C., Corona-Chávez, P., García-Sánchez, L., Sosa-Ceballos, G., & Vázquez, R. (2016). Preliminary report on the July 10–11, 2015 eruption at Volcán de Colima : Pyroclastic density currents with exceptional runouts and volume. Journal of Volcanology and Geothermal Research, 310, 39-49. https://doi.org/10.1016/j.jvolgeores.2015.11.022

Capra, L., Sulpizio, R., Márquez-Ramirez, V. H., Coviello, V., Doronzo, D. M., Arambula-Mendoza, R., & Cruz, S. (2018). The anatomy of a pyroclastic density current : The 10 July 2015 event at Volcán de Colima (Mexico). Bulletin of Volcanology, 80(4), 34. https://doi.org/10.1007/s00445-018-1206-4

Carr, B. B., Clarke, A. B., & Vanderkluysen, L. (2016). The 2006 lava dome eruption of Merapi Volcano (Indonesia) : Detailed analysis using MODIS TIR. Journal of Volcanology and Geothermal Research, 311, 60-71. https://doi.org/10.1016/j.jvolgeores.2015.12.004

Carrara, A., Pinel, V., Bascou, P., Chaljub, E., & De la Cruz-Reyna, S. (2019). Post-emplacement dynamics of andesitic lava flows at Volcán de Colima, Mexico, revealed by radar and optical remote sensing data. Journal of Volcanology and Geothermal Research, 381, 1-15. https://doi.org/10.1016/j.jvolgeores.2019.05.019

Chen, C. W., & Zebker, H. A. (2001). Two-dimensional phase unwrapping with use of statistical models for cost functions in nonlinear optimization. Journal of the Optical Society of America A, 18(2), 338. https://doi.org/10.1364/JOSAA.18.000338

Darmawan, H., Walter, T. R., Brotopuspito, K. S., Subandriyo, & I Gusti Made Agung Nandaka. (2018). Morphological and structural changes at the Merapi lava dome monitored in 2012–15 using unmanned aerial vehicles (UAVs). Journal of Volcanology and Geothermal Research, 349, 256-267. https://doi.org/10.1016/j.jvolgeores.2017.11.006

Darmawan, H., Yuliantoro, P., Suryanto, W., Rakhman, A., & Budi Santoso, A. (2020). Deformation and instability at Merapi dome identified by high resolution camera. IOP Conference Series: Earth and Environmental Science, 500(1), 012008. https://doi.org/10.1088/1755-1315/500/1/012008

Diefenbach, A. K., Bull, K. F., Wessels, R. L., & McGimsey, R. G. (2013). Photogrammetric monitoring of lava dome growth during the 2009 eruption of Redoubt Volcano. Journal of Volcanology and Geothermal Research, 259, 308-316. https://doi.org/10.1016/j.jvolgeores.2011.12.009

Diefenbach, A. K., Crider, J. G., Schilling, S. P., & Dzurisin, D. (2012). Rapid, low-cost photogrammetry to monitor volcanic eruptions: An example from Mount St. Helens, Washington, USA. Bulletin of Volcanology, 74(2), 579-587. https://doi.org/10.1007/s00445-011-0548-y

Dietterich, H. R., Diefenbach, A. K., Soule, S. A., Zoeller, M. H., Patrick, M. P., Major, J. J., & Lundgren, P. R. (2021). Lava effusion rate evolution and erupted volume during the 2018 Kīlauea lower East Rift Zone eruption. Bulletin of Volcanology, 83(4), 25. https://doi.org/10.1007/s00445-021-01443-6

Donnadieu, F., Kelfoun, K., van Wyk de Vries, B., Cecchi, E., & Merle, O. (2003). Digital photogrammetry as a tool in analogue modelling: Applications to volcano instability. Journal of Volcanology and Geothermal Research, 123(1-2), 161-180. https://doi.org/10.1016/S0377-0273(03)00034-9

d'Oreye, N., Derauw, D., Samsonov, S., Jaspard, M., & Smittarello, D. (2021). MasTer: A Full Automatic Multi-Satellite InSAR Mass Processing Tool for Rapid Incremental 2D Ground Deformation Time Series. 2021 IEEE International Geoscience and Remote Sensing Symposium IGARSS, 1899-1902. https://doi.org/10.1109/IGARSS47720.2021.9553615

Ebmeier, S. K., Biggs, J., Mather, T. A., Elliott, J. R., Wadge, G., & Amelung, F. (2012). Measuring large topographic change with InSAR: Lava thicknesses, extrusion rate and subsidence rate at Santiaguito volcano, Guatemala. Earth and Planetary Science Letters, 335-336, 216-225. https://doi.org/10.1016/j.epsl.2012.04.027

Fink. (1998). Morphology, eruption rates, and rheology of lava domes: Insights from laboratory models.

Gertisser, R., Charbonnier, S. J., Keller, J., & Quidelleur, X. (2012). The geological evolution of Merapi volcano, Central Java, Indonesia. Bulletin of Volcanology, 74(5), 1213-1233. https://doi.org/10.1007/s00445-012-0591-3

Goldstein, R. M., & Werner, C. L. (1998). Radar interferogram filtering for geophysical applications. Geophysical Research Letters, 25(21), 4035-4038. https://doi.org/10.1029/1998GL900033

Gouhier, M., Pinel, V., Belart, J. M. C., De Michele, M., Proy, C., Tinel, C., Berthier, E., Guéhenneux, Y., Gudmundsson, M. T., Óskarsson, B. V., Gremion, S., Raucoules, D., Valade, S., Massimetti, F., & Oddsson, B. (2022). CNES-ESA satellite contribution to the operational monitoring of volcanic activity : The 2021 Icelandic eruption of Mt. Fagradalsfjall. Journal of Applied Volcanology, 11(1), 10. https://doi.org/10.1186/s13617-022-00120-3

Fritz, T., Bräutigam, B., Krieger, G., & Zink, M. (2012). TanDEM-X ground segment. TanDEMX experimental product description. Remote Sensing Technology Institute (TD-GS-PS- 3028).

Gleyzes, M. A., Perret, L., & Kubik, P. (2012). Pleiades system architecture and main performances. International Archives of the Photogrammetry, Remote Sensing and Spatial Information Sciences, 39(1), 537-542.

M. Gouhier, V. Pinel, J. M.C. Belart, M. De Michele, C. Proy, C. Tinel, E. Berthier, Y. Guéhenneux, M. T. Gudmundsson, B. V. Oskarsson, S. Gremion, D. Raucoules, S. Valade, F. Massimetti, B. Oddsson, CNES-ESA satellite contribution to the operational monitoring of volcanic activity: The 2021 Icelandic eruption of Mt. Fagradalsfjall, submitted to Applied Volcanology.

Granados-Bolaños, S., Quesada-Román, A., & Alvarado, G. E. (2021). Low-cost UAV applications in dynamic tropical volcanic landforms. Journal of Volcanology and Geothermal Research, 410, 107143. https://doi.org/10.1016/j.jvolgeores.2020.107143

Harnett, C. E., & Heap, M. J. (2021). Mechanical and topographic factors influencing lava dome growth and collapse. Journal of Volcanology and Geothermal Research, 420, 107398. https://doi.org/10.1016/j.jvolgeores.2021.107398

Harnett, C. E., Thomas, M. E., Purvance, M. D., & Neuberg, J. (2018). Using a discrete element approach to model lava dome emplacement and collapse. Journal of Volcanology and Geothermal Research, 359, 68-77. https://doi.org/10.1016/j.jvolgeores.2018.06.017

Harris, A. J. L., & Ripepe, M. (2007). Regional earthquake as a trigger for enhanced volcanic activity : Evidence from MODIS thermal data. Geophysical Research Letters, 34(2), L02304. https://doi.org/10.1029/2006GL028251

Hooper, A., Zebker, H., Segall, P., & Kampes, B. (2004). A new method for measuring deformation on volcanoes and other natural terrains using InSAR persistent scatterers : a new persistent scatterers method. Geophysical Research Letters, 31(23). https://doi.org/10.1029/2004GL021737

Hort, M., Vöge, M., Seyfried, R., & Ratdomopurbo, A. (2006). In situ observation of dome instabilities at Merapi volcano, Indonesia : A new tool for volcanic hazard mitigation. Journal of Volcanology and Geothermal Research, 153(3-4), 301-312. https://doi.org/10.1016/j.jvolgeores.2005.12.007

Kelfoun, K., Santoso, A. B., Latchimy, T., Bontemps, M., Nurdien, I., Beauducel, F., Fahmi, A., Putra, R., Dahamna, N., Laurin, A., Rizal, M. H., Sukmana, J. T., & Gueugneau, V. (2021). Growth and collapse of the 2018–2019 lava dome of Merapi volcano. Bulletin of Volcanology, 83(2), 8. https://doi.org/10.1007/s00445-020-01428-x

Komorowski, J.-C., Jenkins, S., Baxter, P. J., Picquout, A., Lavigne, F., Charbonnier, S., Gertisser, R., Preece, K., Cholik, N., Budi-Santoso, A., & Surono. (2013). Paroxysmal dome explosion during the Merapi 2010 eruption: Processes and facies relationships of associated high-energy pyroclastic density currents. Journal of Volcanology and Geothermal Research, 261, 260-294. https://doi.org/10.1016/j.jvolgeores.2013.01.007

Krieger, G., Moreira, A., Fiedler, H., Hajnsek, I., Werner, M., Younis, M., & Zink, M. (2007). TanDEM-X: A Satellite Formation for High-Resolution SAR Interferometry. IEEE Transactions on Geoscience and Remote Sensing, 45(11), 3317-3341. https://doi.org/10.1109/TGRS.2007.900693

Kubanek, J., Poland, M. P., & Biggs, J. (2021). Applications of Bistatic Radar to Volcano Topography —A Review of Ten Years of TanDEM-X. IEEE Journal of Selected Topics in Applied Earth Observations and Remote Sensing, 14, 3282-3302. https://doi.org/10.1109/JSTARS.2021.3055653

Kubanek, J., Westerhaus, M., & Heck, B. (2017). TanDEM-X Time Series Analysis Reveals Lava Flow Volume and Effusion Rates of the 2012-2013 Tolbachik, Kamchatka Fissure Eruption: The 2012-2013 Tolbachik eruption studied with TanDEM-X. Journal of Geophysical Research: Solid Earth, 122(10), 7754-7774. https://doi.org/10.1002/2017JB014309

Kubanek, J., Westerhaus, M., Schenk, A., Aisyah, N., Brotopuspito, K. S., & Heck, B. (2015). Volumetric change quantification of the 2010 Merapi eruption using TanDEM-X InSAR. Remote Sensing of Environment, 164, 16-25. https://doi.org/10.1016/j.rse.2015.02.027

Lavigne, F., Thouret, J. C., Voight, B., Suwa, H., & Sumaryono, A. (2000). Lahars at Merapi volcano, Central Java: An overview. Journal of Volcanology and Geothermal Research, 100(1-4), 423-456. https://doi.org/10.1016/S0377-0273(00)00150-5

Lundgren, P. R., Bagnardi, M., & Dietterich, H. (2019). Topographic Changes During the 2018 Kīlauea Eruption From Single-Pass Airborne InSAR. Geophysical Research Letters, 46(16), 9554-9562. https://doi.org/10.1029/2019GL083501

Major, J. J., Dzurisin, D., Schilling, S. P., & Poland, M. P. (2009). Monitoring lava-dome growth during the 2004–2008 Mount St. Helens, Washington, eruption using oblique terrestrial photography. Earth and Planetary Science Letters, 286(1-2), 243-254. https://doi.org/10.1016/j.epsl.2009.06.034

Milillo, P., Sacco, G., Di Martire, D., & Hua, H. (2022). Neural Network Pattern Recognition Experiments Toward a Fully Automatic Detection of Anomalies in InSAR Time Series of Surface Deformation. Frontiers in Earth Science, 9, 728643. https://doi.org/10.3389/feart.2021.728643

Moussallam, Y., Barnie, T., Amigo, Á., Kelfoun, K., Flores, F., Franco, L., Cardona, C., Cordova, L., & Toloza, V. (2021). Monitoring and forecasting hazards from a slow growing lava dome using aerial imagery, tri-stereo Pleiades-1A/B imagery and PDC numerical simulation. Earth and Planetary Science Letters, 564, 116906. https://doi.org/10.1016/j.epsl.2021.116906

Newhall, C. G., Bronto, S., Alloway, B., Banks, N. G., Bahar, I., del Marmol, M. A., Hadisantono, R. D., Holcomb, R. T., McGeehin, J., Miksic, J. N., Rubin, M., Sayudi, S. D., Sukhyar, R.,

Andreastuti, S., Tilling, R. I., Torley, R., Trimble, D., & Wirakusumah, A. D. (2000). 10,000Years of explosive eruptions of Merapi Volcano, Central Java : Archaeological and modern implications. Journal of Volcanology and Geothermal Research, 100(1-4), 9-50. https://doi.org/10.1016/S0377-0273(00)00132-3

Newhall, C. G., & Melson, W. G. (1983a). Explosive activity associated with the growth of volcanic domes. Journal of Volcanology and Geothermal Research, 17(1-4), 111-131. https://doi.org/10.1016/0377-0273(83)90064-1

Newhall, C. G., & Melson, W. G. (1983b). Explosive activity associated with the growth of volcanic domes. Journal of Volcanology and Geothermal Research, 17(1-4), 111-131. https://doi.org/10.1016/0377-0273(83)90064-1

Ogburn, S. E., Loughlin, S. C., & Calder, E. S. (2015). The association of lava dome growth with major explosive activity (VEI ≥ 4) : DomeHaz, a global dataset. Bulletin of Volcanology, 77(5), 40. https://doi.org/10.1007/s00445-015-0919-x

Ordoñez, M., Laverde, C., & Battaglia, M. (2022). The new lava dome growth of Nevado del Ruiz (2015–2021). Journal of Volcanology and Geothermal Research, 430, 107626. https://doi.org/10.1016/j.jvolgeores.2022.107626

Pallister, J. S., Schneider, D. J., Griswold, J. P., Keeler, R. H., Burton, W. C., Noyles, C., Newhall, C. G., & Ratdomopurbo, A. (2013). Merapi 2010 eruption—Chronology and extrusion rates monitored with satellite radar and used in eruption forecasting. Journal of Volcanology and Geothermal Research, 261, 144-152. https://doi.org/10.1016/j.jvolgeores.2012.07.012

G. B. M. Pedersen, J. M. C. Belart, M. T. Guðmundsson, B. V. Óskarsson, N. Gies, Þ. Högnadóttir, Á. R. Hjartardóttir, V. Pinel, E. Berthier ,T. Durig, H. I. Reynolds, C. W. Hamilton, G. Valsson, P. Einarsson, D. Ben-Yehosua A. Gunnarsson, B. Oddsson, Volume, discharge rate and lava transport at the Fagradalsfjall eruption 2021: Results from near-real time photogrammetric monitoring, in revision for GRL. Preprint available here: https://www.essoar.org/doi/10.1002/essoar.10509177.1

Pinel, V., Beauducel, F., Putra, R., Sulistiyani, S., Nandaka, G. M. A., Nurnaning, A., Budi Santoso, A., Humaida, H., Doin, M.-P., Thollard, F., & Laurent, C. (2021). Monitoring of Merapi volcano, Indonesia based on Sentinel-1 data [Other]. pico. https://doi.org/10.5194/egusphere-egu21-10392

Poland, M. P. (2014). Time-averaged discharge rate of subaerial lava at Kīlauea Volcano, Hawai‘i, measured from TanDEM-X interferometry : Implications for magma supply and storage during 2011-2013: Lava effusion at Kīlauea from TanDEM-X. Journal of Geophysical Research: Solid Earth, 119(7), 5464-5481. https://doi.org/10.1002/2014JB011132

QGIS Development Team, 2022. QGIS Geographic Information System. Open Source Geospatial Foundation. URL http://qgis.org

Ratdomopurbo, A., & Poupinet, G. (2000). An overview of the seismicity of Merapi volcano (Java, Indonesia), 1983–1994. Journal of Volcanology and Geothermal Research, 100(1-4), 193-214. https://doi.org/10.1016/S0377-0273(00)00137-2

Ratdomopurbo, A., Beauducel, F., Subandriyo, J., Agung Nandaka, I. G. M., Newhall, C. G., Suharna, Sayudi, D. S., Suparwaka, H., & Sunarta. (2013). Overview of the 2006 eruption of Mt. Merapi. Journal of Volcanology and Geothermal Research, 261, 87-97. https://doi.org/10.1016/j.jvolgeores.2013.03.019

Richter, N., Poland, M. P., & Lundgren, P. R. (2013). TerraSAR-X interferometry reveals small-scale deformation associated with the summit eruption of Kīlauea Volcano, Hawai'i : small-scale deformation from TSX InSAR. Geophysical Research Letters, 40(7), 1279-1283. https://doi.org/10.1002/grl.50286

Rosen, P. A., Hensley, S., Peltzer, G., & Simons, M. (2004). Updated repeat orbit interferometry package released. Eos, Transactions American Geophysical Union, 85(5), 47-47. https://doi.org/10.1029/2004EO050004

Rowland, S. K., Harris, A. J. L., Wooster, M. J., Amelung, F., Garbeil, H., Wilson, L., & Mouginis-Mark, P. J. (2003). Volumetric characteristics of lava flows from interferometric radar and multispectral satellite data : The 1995 Fernandina and 1998 Cerro Azul eruptions in the western Galapagos. Bulletin of Volcanology, 65(5), 311-330. https://doi.org/10.1007/s00445-002-0262-x

Ryan, G. A., Loughlin, S. C., James, M. R., Jones, L. D., Calder, E. S., Christopher, T., Strutt, M. H., & Wadge, G. (2010). Growth of the lava dome and extrusion rates at Soufrière Hills Volcano, Montserrat, West Indies : 2005-2008: extrusion rates at Soufrière Hills. Geophysical Research Letters, 37(19), n/a-n/a. https://doi.org/10.1029/2009GL041477

Salzer, J. T., Milillo, P., Varley, N., Perissin, D., Pantaleo, M., & Walter, T. R. (2017). Evaluating links between deformation, topography and surface temperature at volcanic domes : Results from a multi-sensor study at Volcán de Colima, Mexico. Earth and Planetary Science Letters, 479, 354-365. https://doi.org/10.1016/j.epsl.2017.09.027

Shean, D. E., Alexandrov, O., Moratto, Z. M., Smith, B. E., Joughin, I. R., Porter, C., & Morin, P. (2016). An automated, open-source pipeline for mass production of digital elevation models (DEMs) from very-high-resolution commercial stereo satellite imagery. ISPRS Journal of Photogrammetry and Remote Sensing, 116, 101-117. https://doi.org/10.1016/j.isprsjprs.2016.03.012

Siswowidjoyo, S., Suryo, I., & Yokoyama, I. (1995). Magma eruption rates of Merapi volcano, Central Java, Indonesia during one century (1890–1992). Bulletin of Volcanology, 57(2), 111-116. https://doi.org/10.1007/BF00301401

Solikhin, A., Pinel, V., Vandemeulebrouck, J., Thouret, J.-C., & Hendrasto, M. (2015). Mapping the 2010 Merapi pyroclastic deposits using dual-polarization Synthetic Aperture Radar (SAR) data. Remote Sensing of Environment, 158, 180-192. https://doi.org/10.1016/j.rse.2014.11.002

Sparks. (1998). Magma production and growth of the lava dome of the Soufriere November Hills Volcano, 1995 to Montserrat, December West Indies : 1997.

Stumpf, A., Malet, J.-P., Allemand, P., & Ulrich, P. (2014). Surface reconstruction and landslide displacement measurements with Pléiades satellite images. ISPRS Journal of Photogrammetry and Remote Sensing, 95, 1-12. https://doi.org/10.1016/j.isprsjprs.2014.05.008

Surono, Jousset, P., Pallister, J., Boichu, M., Buongiorno, M. F., Budisantoso, A., Costa, F., Andreastuti, S., Prata, F., Schneider, D., Clarisse, L., Humaida, H., Sumarti, S., Bignami, C., Griswold, J., Carn, S., Oppenheimer, C., & Lavigne, F. (2012). The 2010 explosive eruption of Java's Merapi volcano—A '100-year' event. Journal of Volcanology and Geothermal Research, 241-242, 121-135. https://doi.org/10.1016/j.jvolgeores.2012.06.018

Thiele, S. T., Varley, N., & James, M. R. (2017). Thermal photogrammetric imaging : A new technique for monitoring dome eruptions. Journal of Volcanology and Geothermal Research, 337, 140-145. https://doi.org/10.1016/j.jvolgeores.2017.03.022

Voight, B., Constantine, E. K., Siswowidjoyo, S., & Torley, R. (2000). Historical eruptions of Merapi Volcano, Central Java, Indonesia, 1768–1998. Journal of Volcanology and Geothermal Research, 100(1-4), 69-138. https://doi.org/10.1016/S0377-0273(00)00134-7

Wadge, G., Cole, P., Stinton, A., Komorowski, J.-C., Stewart, R., Toombs, A. C., & Legendre, Y. (2011). Rapid topographic change measured by high-resolution satellite radar at Soufriere Hills Volcano, Montserrat, 2008–2010. Journal of Volcanology and Geothermal Research, 199(1-2), 142-152. https://doi.org/10.1016/j.jvolgeores.2010.10.011

Wadge, G., Macfarlane, D. G., Odbert, H. M., James, M. R., Hole, J. K., Ryan, G., Bass, V., De Angelis, S., Pinkerton, H., Robertson, D. A., & Loughlin, S. C. (2008). Lava dome growth and mass wasting measured by a time series of ground-based radar and seismicity observations : growth of a lava dome and talus. Journal of Geophysical Research: Solid Earth, 113(B8). https://doi.org/10.1029/2007JB005466

Walter, T. R. (2011). Low cost volcano deformation monitoring : Optical strain measurement and application to Mount St. Helens data. Geophysical Journal International, 186(2), 699-705. https://doi.org/10.1111/j.1365-246X.2011.05051.x

Walter, T. R., Legrand, D., Granados, H. D., Reyes, G., & Arámbula, R. (2013a). Volcanic eruption monitoring by thermal image correlation : Pixel offsets show episodic dome growth of the Colima volcano. Journal of Geophysical Research: Solid Earth, 118(4), 1408-1419. https://doi.org/10.1002/jgrb.50066

Walter, T. R., Ratdomopurbo, A., Subandriyo, Aisyah, N., Brotopuspito, K. S., Salzer, J., & Lühr, B. (2013b). Dome growth and coulée spreading controlled by surface morphology, as determined by pixel offsets in photographs of the 2006 Merapi eruption. Journal of Volcanology and Geothermal Research, 261, 121-129. https://doi.org/10.1016/j.jvolgeores.2013.02.004

Walter, T. R., Subandriyo, J., Kirbani, S., Bathke, H., Suryanto, W., Aisyah, N., Darmawan, H., Jousset, P., Luehr, B.-G., & Dahm, T. (2015). Volcano-tectonic control of Merapi's lava dome splitting : The November 2013 fracture observed from high resolution TerraSAR-X data. Tectonophysics, 639, 23-33. https://doi.org/10.1016/j.tecto.2014.11.007

Walter, T. R., Harnett, C. E., Varley, N., Bracamontes, D. V., Salzer, J., Zorn, E. U., Bretón, M., Arámbula, R., & Thomas, M. E. (2019). Imaging the 2013 explosive crater excavation and new dome formation at Volcán de Colima with TerraSAR-X, time-lapse cameras and modelling. Journal of Volcanology and Geothermal Research, 369, 224-237. https://doi.org/10.1016/j.jvolgeores.2018.11.016

Walter, T. R., Zorn, E. U., Harnett, C. E., Shevchenko, A. V., Belousov, A., Belousova, M., & Vassileva, M. S. (2022). Influence of conduit and topography complexity on spine extrusion at Shiveluch volcano, Kamchatka. Communications Earth & Environment, 3(1), 169. https://doi.org/10.1038/s43247-022-00491-w

Wang, T., Poland, M. P., & Lu, Z. (2015). Dome growth at Mount Cleveland, Aleutian Arc, quantified by time series TerraSAR-X imagery : dome growth from SAR amplitude features. Geophysical Research Letters, 42(24), 10,614-10,621. https://doi.org/10.1002/2015GL066784

Yoon, Y. T., Eineder, M., Yague-Martinez, N., & Montenbruck, O. (2009). TerraSAR-X Precise Trajectory Estimation and Quality Assessment. IEEE Transactions on Geoscience and Remote Sensing, 47(6), 1859-1868. https://doi.org/10.1109/TGRS.2008.2006983

Zink, M., Bachmann, M., Brautigam, B., Fritz, T., Hajnsek, I., Moreira, A., Wessel, B., & Krieger, G. (2014). TanDEM-X : The New Global DEM Takes Shape. IEEE Geoscience and Remote Sensing Magazine, 2(2), 8-23. https://doi.org/10.1109/MGRS.2014.2318895

Zorn, E. U., Walter, T. R., Johnson, J. B., & Mania, R. (2020). UAS-based tracking of the Santiaguito Lava Dome, Guatemala. Scientific Reports, 10(1), 8644. https://doi.org/10.1038/s41598-020-65386-2

Zorn, E. U., Le Corvec, N., Varley, N. R., Salzer, J. T., Walter, T. R., Navarro-Ochoa, C., Vargas-Bracamontes, D. M., Thiele, S. T., & Arámbula Mendoza, R. (2019). Load Stress Controls on Directional Lava Dome Growth at Volcán de Colima, Mexico. Frontiers in Earth Science, 7, 84. https://doi.org/10.3389/feart.2019.00084